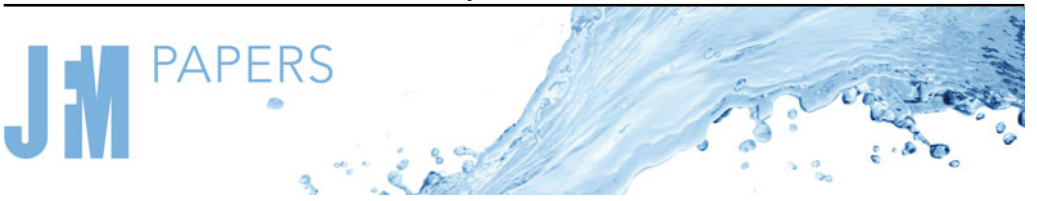
J. Fluid Mech. (2025), *vol.* 1020, A29, doi:10.1017/jfm.2025.10514



Attenuating transmitted infragravity waves by a small heaving body

Lidong Cui[1], **Luke G. Bennetts**[2], **Amy-Rose Westcott**[3], **Justin S. Leontini**[1], **Nataliia Y. Sergiienko**[4], **Benjamin S. Cazzolato**[4] and **Richard Manasseh**[1]

[1]Department of Mechanical and Product Design Engineering, Swinburne University of Technology, Hawthorn, VIC 3122, Australia

[2]School of Mathematics and Statistics, The University of Melbourne, Parkville, VIC 3010, Australia

[3]School of Computer and Mathematical Sciences, The University of Adelaide, Adelaide, SA 5005, Australia

[4]School of Electrical and Mechanical Engineering, The University of Adelaide, Adelaide, SA 5005, Australia

Corresponding author: Lidong Cui, lcui@swin.edu.au

(Received 14 April 2025; revised 16 June 2025; accepted 21 July 2025)

When a water wave group encounters a floating body, it forces the body into motion; this motion radiates waves that modify the wave group. This study considers a floating body in the form of a two-dimensional (2-D) rectangular block constrained to heaving motion. The focus is on how the 2-D block modifies infragravity (*IG*) waves, a type of nonlinear low-frequency wave in the wave group. The *IG* waves transmitted beyond the block comprise two types: (i) bound *IG* waves generated by nonlinear interactions of first-order carrier waves, and (ii) free *IG* waves released due to discontinuities in flow potential created by the block. A systematic parameter sweep reveals that, when heaving motion is allowed, the transmitted *IG* waves differ significantly from those of stationary blocks. In some cases, heaving motion enables attenuation of the total transmitted *IG* waves, while stationary blocks cannot achieve similar effects. Only small-sized blocks are considered; they are 'small' compared with the *IG* wavelengths. The findings are relevant to dual-purpose wave energy converters designed for energy generation and coastal protection, floating breakwaters and other small-sized floating structures such as ships and some icebergs: the heaving motion of these objects may modify *IG* waves, thereby influencing harbour resonance, near-shore currents, beach erosion, wave forcing on ice shelves and coastal inundation.

Key words: wave-structure interactions, surface gravity waves, wave scattering

© The Author(s), 2025. Published by Cambridge University Press. This is an Open Access article, distributed under the terms of the Creative Commons Attribution licence (https://creativecommons.org/licenses/by/4.0/), which permits unrestricted re-use, distribution and reproduction, provided the original article is properly cited.

https://doi.org/10.1017/jfm.2025.10514 Published online by Cambridge University Press

1. Introduction

1.1. *Background and motivation*

Infragravity waves (*IG* waves), as oceanic surface waves, are generally of small steepness (e.g. Ardhuin, Rawat & Aucan 2014), yet they can be impactful (Bertin *et al.* 2018). Their periods (approximately 30–300 s) are much greater than dominant wind-generated surface gravity waves, enabling them to resonantly excite harbours, thus disrupt maritime operations (Bowers 1977; Mei & Agnon 1989; Wu & Liu 1990) and affect large ships (Agnon, Choi & Mei 1988), whose natural periods are commensurate with those of *IG* waves. The *IG* waves also influence coastal processes, including beach morphodynamics and coastal flooding events (§ 4, Bertin *et al.* 2018). In addition, *IG* waves play roles in ice shelf disintegration (e.g. Bennetts, Liang & Pitt 2022), thereby indirectly affecting sea level and climate dynamics. Because of these, controlling *IG* waves is sometimes necessary.

A canonical model for studying *IG* waves is nonlinear interactions between two monochromatic carrier waves of slightly different frequencies (Longuet-Higgins & Stewart 1962; Mei, Stiassnie & Yue 2005). The carrier waves are assumed to travel in the same direction, forming a wave group with group speed C_g. Let the frequencies of the carrier waves be f_1 and f_2, then the associated *IG* wave frequency is $|f_1 - f_2|$. The speed of such an *IG* wave is C_g, as if it is 'bound' to the carrier wave group. For this reason, it is named in the literature as a bound *IG* wave, or phase-locked *IG* wave; see the red curve in figure 1 for an example.

It is well known from early studies (e.g. Longuet-Higgins & Stewart 1962) that the amplitude of the bound *IG* wave is related to the product of the amplitudes of carrier waves (see 4.3). When the carrier waves are altered by an obstacle, so are the bound *IG* waves (e.g. Liu & Iskandarani 1991). However, attenuation of bound *IG* waves does not ensure reduction of total *IG* waves, because a change of bound *IG* waves creates a discontinuity in the *IG* wave's flow potential, and to rectify the discontinuity, free *IG* waves are required (e.g. Agnon & Mei 1985; Mei & Agnon 1989; Wu & Liu 1990; Liu & Iskandarani 1991; Bertin *et al.* 2018). The resulting total *IG* wave (free plus bound *IG* waves) is not necessarily smaller than the incident bound *IG* waves. A well-known added complication is that the free *IG* waves travel at the phase velocity appropriate to waves satisfying the linear solution, which is generally faster than bound *IG* waves. These lead to spatial modulation of the total *IG* wave amplitude, i.e. oscillations in the total *IG* wave amplitude on the lee side of an obstacle, which is well established for some types of obstacles (e.g. Massel 1983; Agnon & Mei 1985; Li *et al.* 2021) although not for the heaving blocks to be investigated in this work.

Despite these complications, some means of *IG* wave control have been developed. Some ideas require permanent and significant maritime infrastructure, e.g. fixed breakwaters that block a broad spectrum of the wave energy (McComb, Johnson & Beamsley 2009), or Bragg-scattering bathymetry (Gao *et al.* 2021). Smaller structures, whose characteristic dimensions are much less than the wavelength of *IG* waves, are usually optimised for interacting with linear carrier waves, but not *IG* waves. Typical examples of such small structures include wave energy converters (WECs, e.g. Falnes & Kurniawan 2020), and many prototype WECs are heaving resonators (e.g. Westcott *et al.* 2024). A recent study (Sergiienko *et al.* 2024) explored, experimentally, whether such heaving resonators can also modify *IG* waves. It was observed that the total *IG* wave amplitudes are reduced in the lee of arrays of WECs. The WECs used by Sergiienko *et al.* (2024) are quasi-infinite rows of oscillating water columns (OWCs), represented by straight surface-piercing cylindrical pipes with open ends immersed in the water.

https://doi.org/10.1017/jfm.2025.10514 Published online by Cambridge University Press

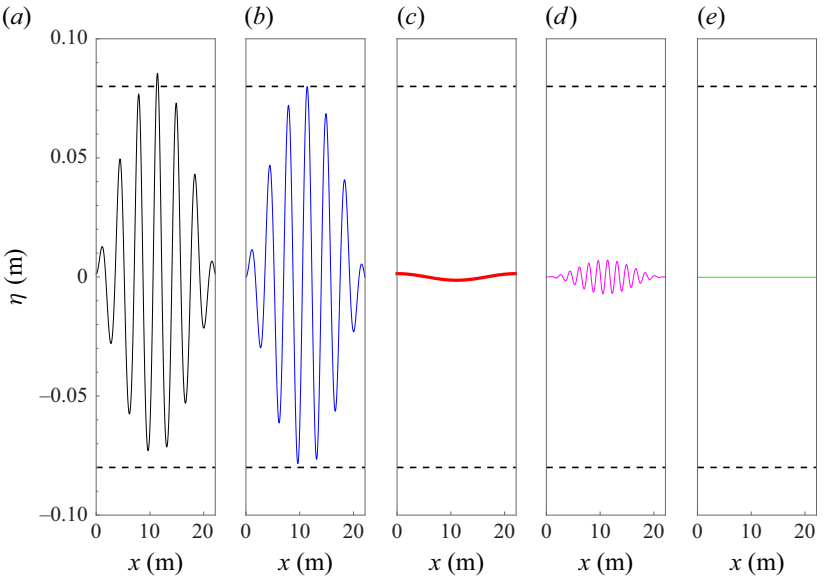


Figure 1. (*a*) Surface elevation of a typical nonlinear wave group discussed in this paper. The wave group is constituted by the four components shown in (*b–d*). They are: (*b*) first-order (linear) carrier wave group containing two linear waves with $f_1 = 0.617$ Hz, $f_2 = 1.1 f_1$ and $A_1 = A_2 = 0.04$ m; (*c*) second-order low-frequency bound waves (i.e. *IG* waves), (*d*) second-order high-frequency bound waves and (*e*) a 'set-down' (i.e. a depression of the mean free surface; the 'set-down' in this case is nearly zero). Water depth $h = 1$ m.

The radius of these OWCs is much smaller than both the *IG* and carrier waves, and their natural frequencies are tuned to the carrier wave frequencies.

1.2. *Motivation and scope*

Motivated by the experimental results in Sergiienko *et al.* (2024), the current study discusses the effects of small-sized heaving bodies on *IG* waves analytically, intending to provide a phenomenological, qualitative explanation of the *IG* wave reduction by OWCs. The heaving bodies in this paper are represented by two-dimensional (2-D) floating rectangular blocks allowed to heave. Although the cylindrical OWC arrays used in Sergiienko *et al.* (2024) are by no means rectangular blocks, they share similarities: (i) the up-and-down motion of the water in the OWCs is akin to the heaving motion of a rigid 'piston' (e.g. Sheng, Alcorn & Lewis 2014); (ii) when the spacing between OWCs is small enough, as it is the case in Sergiienko *et al.* (2024), the wave field around the OWC rows is quasi-two-dimensional, akin to the behaviour of waves around 2-D rectangular blocks. 'Quasi-two-dimensional' means the wave's propagating modes have no variation on the spanwise direction (Srokosz 1980; Falnes & Budal 1982). The current study can also be related to other objects, such as other types of WECs, floating breakwaters, ships and icebergs (concerning their heaving motions).

Similar to Sergiienko *et al.* (2024) and all papers to be reviewed in this section, the present study assumes that the incident wave field only consists of carrier wave groups and associated bound *IG* waves, i.e. there exist no incident (pre-existing) free *IG* waves from a distant source. This scenario is relevant to harbours and coasts where the unwanted free *IG* waves are released locally when the incident carrier wave groups interact with local bathymetry features (Elgar *et al.* 1992) such as reef platforms (McComb *et al.* 2009). For these cases, interventions, such as the WECs proposed by Sergiienko *et al.* (2024), can

https://doi.org/10.1017/jfm.2025.10514 Published online by Cambridge University Press

be placed upwave of the bathymetry features to modify the incident wave field before it interacts with the bathymetry features. If the *IG* wave field is dominated by significant free *IG* waves originating from a distant location, the small devices are unlikely to be effective.

Also similar to Sergiienko *et al.* (2024), in this work, the natural frequency of the 2-D block's heaving motion will be tuned to be close to the carrier waves' frequencies, which are an order of magnitude higher than the *IG* wave's frequencies. This allows the size of the blocks to be much smaller than the *IG* wavelength.

A wide range of parameters will be explored; this is an improvement over Sergiienko *et al.* (2024), which studied only a few cases due to the restriction of the wave flume: a more systematic experimental study involving *IG* waves is time consuming and resource demanding: longer wave flumes and longer setting times between experiments are needed if longer *IG* waves are to be studied.

1.3. *Methodology and paper structure*

The analytical method used in this paper is an extension of some past studies. Agnon & Mei (1985) and Agnon *et al.* (1988) used a multiple-scale method to analyse second-order sway ('slow drift') motion of floating blocks, such as large ships, caused by *IG* waves. Their focus was primarily on the force caused by *IG* waves, not on *IG* wave reduction as in the present work; moreover, heaving was not discussed. Using a reduced version of the methods in Agnon & Mei (1985), a 2-D stationary plate suspended in the water is considered by Liu & Iskandarani (1991), who focused on *IG* wave attenuation. They discovered that, although the bound *IG* waves are reduced when the incident carrier waves are reduced, free *IG* waves are released at the devices, offsetting the bound *IG* wave reduction, indicating the stationary plates discussed in the paper are not suitable devices for total *IG* wave reduction. Two key assumptions are invoked by Liu & Iskandarani (1991): (i) the plate's characteristic length is much smaller than the *IG* waves, enabling the Froude–Krylov-like assumption (e.g. McCormick 2009, § 11.3) for treating *IG* waves, such that the pressure field of the *IG* wave is not affected by the presence of a small-sized object; and (ii) the *IG* wave potential remains constant across the plate.

Subsequent studies that cite Liu & Iskandarani (1991) are mostly concerned with linear waves, rather than nonlinearly generated *IG* waves. However, four papers focus on *IG* waves using the method of Liu & Iskandarani (1991). These include those who studied fixed vertical thin barriers (Losada, Losada & Roldán 1993), those who studied fixed submerged porous plates (Neves *et al.* 2000*a*) and those who studied fixed semi-infinite breakwaters (Neves *et al.* 2000*b*). In these studies, device motion was not analysed, and the conclusions are similar to Liu & Iskandarani (1991): undesirable free *IG* waves will be released when the bound *IG* waves are reduced at the device. Finally, Hossain, Kioka & Kitano (2001) studied stationary 2-D rectangular blocks (in the context of floating breakwaters) and relaxed the assumption (ii) in Liu & Iskandarani (1991). The main finding was, again, that free *IG* waves will be released whilst the bound *IG* waves are attenuated.

The current work removes the constraint that the device is fixed (stationary), by allowing heaving motion. Such an undertaking does not change the basic mathematical paradigm, but it requires new algebraic details concerning device motion, and yields qualitatively new results that resolve the abovementioned lament *vis-à-vis* the release of free *IG* waves when bound *IG* waves are reduced, hence providing insights into the total *IG* wave reduction observed by Sergiienko *et al.* (2024).

The present paper is organised as follows. In § 2, governing equations and an overview of solution types are presented. Section 3 discusses a 2-D floating rectangular heaving

https://doi.org/10.1017/jfm.2025.10514 Published online by Cambridge University Press

block interacting with the two linear carrier waves by the eigenfunction expansion method (e.g. Linton & McIver 2001). This is followed by § 4, where bound *IG* waves are calculated from carrier wave groups, using a known approach based on a multiple-scale analysis. The algebraic details for the heaving cases will differ from the diffraction-only cases studied by Hossain *et al.* (2001). With bound *IG* waves specified, free *IG* waves are calculated in § 5 with the approach in Liu & Iskandarani (1991). Resolving free waves results in a second-order wave potential underneath the block; this wave potential forces the block to a 'slow' heaving motion, which radiates additional free *IG* waves. Such additional free *IG* waves contribute to *IG* wave modification, see § 6. Some examples related to laboratory conditions are then presented. A sweep over the parameter space is carried out for diffraction-only blocks in § 7. Although these were already studied by Hossain *et al.* (2001), in this study, the parameter range is wider, and the focus is placed on all types of *IG* waves (bound, free and total) instead of only on the free *IG* waves. Examples of heaving blocks are then discussed in § 8. The main new finding is that some blocks can significantly reduce the total *IG* waves for all locations in the lee of the block, a feat not possible with diffraction-only blocks. The relationship between *IG* wave reduction and the linear resonant frequencies of the blocks will be discussed. In § 9, the roles of viscous damping are discussed informally, via an empirical damping term (McCormick 2009). Section 9 further discusses other modulation ratios, as well as an example using parameters related to coastal engineering. Section 9 also presents concluding remarks. Appendix A discusses scaling in perturbation expansion; Appendices B and C provide details on linear diffraction and radiation problems. Appendices D, E and F contain details of lengthy expressions needed in the main text. Appendix G explains why bound *IG* waves can sometimes be amplified by heaving blocks.

2. Governing equations and an overview of solutions

2.1. *Governing equations and boundary conditions*

The assumption of inviscid, irrotational flow is standard for the problem of *IG* wave interaction with structures (e.g. Agnon *et al.* 1988). Under this assumption, let Φ be a scalar flow potential for water waves (Mei *et al.* 2005); it relates to flow velocity $\boldsymbol{u}$ via

$$\boldsymbol{u} = \nabla\Phi = \frac{\partial\Phi}{\partial x}\boldsymbol{i} + \frac{\partial\Phi}{\partial z}\boldsymbol{k}, \tag{2.1}$$

where y-independency is assumed; x and z are spatial variables, $\boldsymbol{i}$ and $\boldsymbol{k}$ are unit vectors along x- and z-axes, respectively, and Φ is governed by the Laplace equation in the fluid domain

$$\frac{\partial^2\Phi}{\partial x^2} + \frac{\partial^2\Phi}{\partial z^2} = 0. \tag{2.2}$$

For the water wave problem, a free surface exists. Let η denote the free-surface elevation; to $O(\eta^2)$, the two free-surface boundary conditions on $z = 0$ are (Mei *et al.* 2005, § 13.2.1)

$$-\mathrm{g}\eta = \left(\frac{\partial\Phi}{\partial t} + \eta\frac{\partial^2\Phi}{\partial t\partial z} + \frac{\eta^2}{2}\frac{\partial}{\partial t}\frac{\partial^2\Phi}{\partial z^2}\right) + \frac{1}{2}\left(\boldsymbol{u}^2 + \eta\frac{\partial\boldsymbol{u}^2}{\partial z}\right)\Bigg|_{z=0}, \tag{2.3}$$

$$\left(\frac{\partial^2\Phi}{\partial t^2} + \mathrm{g}\frac{\partial\Phi}{\partial z}\right) + \eta\left[\frac{\partial}{\partial z}\left(\frac{\partial^2\Phi}{\partial t^2} + \mathrm{g}\frac{\partial\Phi}{\partial z}\right)\right] + \frac{\eta^2}{2}\left[\frac{\partial^2}{\partial z^2}\left(\frac{\partial^2\Phi}{\partial t^2} + \mathrm{g}\frac{\partial\Phi}{\partial z}\right)\right] + \frac{\partial\boldsymbol{u}^2}{\partial t} + \eta\frac{\partial^2\boldsymbol{u}^2}{\partial t\partial z} + \frac{1}{2}\boldsymbol{u}\cdot\nabla\boldsymbol{u}^2 = 0\Bigg|_{z=0}, \tag{2.4}$$

https://doi.org/10.1017/jfm.2025.10514 Published online by Cambridge University Press

where $\mathrm{g} \approx 9.81\ \mathrm{m/s^2}$ is the gravitational acceleration, t is a time variable. For a sea of depth h with a flat bottom, the bottom boundary condition is the no-penetration condition

$$\frac{\partial \Phi}{\partial z} = 0\bigg|_{z=-h}. \tag{2.5}$$

Define a small book-keeping parameter related to wave steepness

$$\varepsilon \equiv k_{0,1} A_1 \ll 1, \tag{2.6}$$

where $k_{0,1}$ is the progressive wavenumber of a carrier wave, A_1 being its amplitude. The unknowns Φ and η are expanded in terms of ε

$$\Phi = \varepsilon \Phi_1 + \varepsilon^2 \Phi_2 + \varepsilon^3 \Phi_3 + \ldots, \tag{2.7}$$

$$\eta = \varepsilon \eta_1 + \varepsilon^2 \eta_2 + \varepsilon^3 \eta_3 + \ldots. \tag{2.8}$$

A multiple-scale method for the water wave problem presumes that x can be separated into a fast variable $\mathfrak{x}$ and a slow variable $X \equiv \varepsilon \mathfrak{x}$, and similarly, t can be separated into a fast time $\mathfrak{t}$ and a slow time $T \equiv \varepsilon \mathfrak{t}$. Hence, in (2.7, 2.8), $\Phi_n (n = 1, 2, 3)$ and η_n, $(n = 1, 2, 3)$ are functions of $(\mathfrak{x}, X, \mathfrak{t}, T, z)$. It should be noted that, in principle, the slow variables X and T should be characterised by a different small parameter other than ε (see e.g. Li *et al.* 2021). However, the use of a single small parameter ε aids clarity, and as explained in Appendix A, it is reasonable for some problems, such as in Benney & Roskes (1969) and the current problem.

Substituting (2.7, 2.8) into the Laplace equation and the boundary conditions, at the leading order $O(\varepsilon)$, one finds the following linear equations for Φ_1 and η_1:

$$\frac{\partial^2 \Phi_1}{\partial \mathfrak{x}^2} + \frac{\partial^2 \Phi_1}{\partial z^2} = 0;\ \ \frac{\partial^2 \Phi_1}{\partial \mathfrak{t}^2} + \mathrm{g}\frac{\partial \Phi_1}{\partial z} = 0\bigg|_{z=0};\ \ -\mathrm{g}\eta_1 = \frac{\partial \Phi_1}{\partial \mathfrak{t}}\bigg|_{z=0};\ \ \frac{\partial \Phi_1}{\partial z} = 0\bigg|_{z=-h}. \tag{2.9}$$

Two types of solutions exist for (2.9). One, a periodic solution that involves only fast variables, e.g. $\Phi_1 = \phi_1(z)\mathrm{e}^{\mathrm{i}(k\mathfrak{x}-\omega \mathfrak{t})}$, the other, a solution in the form of $\Phi_1(X, T)$, containing only slow variables (e.g. Mei *et al.* 2005, (13.2.21)). The former is the classical Airy solution for water waves (e.g. Manasseh 2021), named carrier wave in this paper, while the latter corresponds to a slow-varying solution related to the bound *IG* wave. The function $\Phi_1(X, T)$ is so far an arbitrary function of slow variables; its details cannot be specified at $O(\varepsilon)$. To determine its analytical form, analyses must be carried to $O(\varepsilon^2)$ and $O(\varepsilon^3)$, leading to (4.1), from which $\Phi_1(X, T)$ can be solved.

2.2. *Wave modification due to the heaving body: an overview*

Consider in figure 2, a block of draught d and length $2L$ on a water depth h, allowed to heave. It interacts with a nonlinear wave group containing, among others, two linear carrier waves and a nonlinearly generated bound *IG* wave. The block's linear interaction with two carrier waves η^{I,A_1} and η^{I,A_2} leads to the following surface elevations in region I of figure 2 ($\mathfrak{x} < -L$):

$$\eta^{\mathrm{I},A_1} + \eta^{\mathrm{I},A_2} + \eta^{\mathrm{I},D_1} + \eta^{\mathrm{I},D_2} + \eta^{\mathrm{I},R_1} + \eta^{\mathrm{I},R_2}, \tag{2.10}$$

and the following waves in region III ($\mathfrak{x} > L$):

$$\eta^{\mathrm{III},D_1} + \eta^{\mathrm{III},D_2} + \eta^{\mathrm{III},R_1} + \eta^{\mathrm{III},R_2}, \tag{2.11}$$

where superscripts I and III denote region I and region III. The superscripts A_n, D_n, R_n, $(n = 1, 2)$ denote the first and second approaching (i.e. incident), diffracted, and radiated waves, respectively. These linear waves are determined in § 3.

https://doi.org/10.1017/jfm.2025.10514 Published online by Cambridge University Press

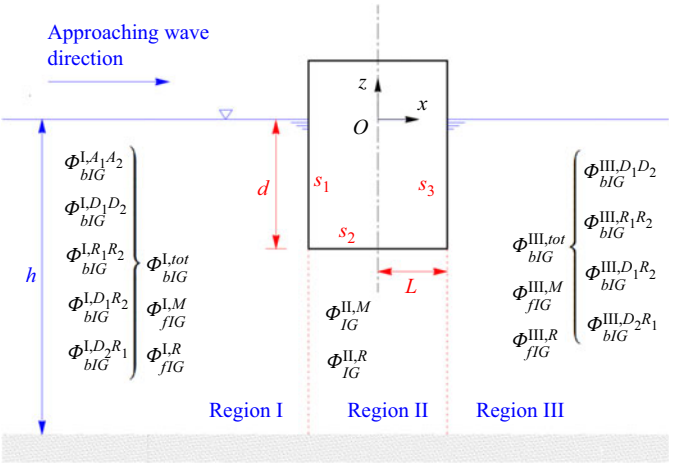


Figure 2. Cross-section of a 2-D rectangular heaving block on a water layer of depth h. The block's resting draught is d, with length $2L$. Regions I, II and III are named to facilitate analysis. Here, $s_{1,2,3}$ are the names of the three immersed surfaces of the 2-D block. Second-order *IG* wave potentials (black fonts) in different regions are also shown. These wave potentials are specified from § 4 to § 6.

Nonlinear interactions between carrier waves spawn a total bound *IG* wave potential denoted by $\Phi^{\mathrm{I},tot}_{bIG}$ in region I (the superscript *tot* means 'total')

$$\Phi^{\mathrm{I},tot}_{bIG} = \Phi^{\mathrm{I},A_1A_2}_{bIG} + \Phi^{\mathrm{I},D_1D_2}_{bIG} + \Phi^{\mathrm{I},R_1R_2}_{bIG} + \Phi^{\mathrm{I},D_1R_2}_{bIG} + \Phi^{\mathrm{I},D_2R_1}_{bIG}, \tag{2.12}$$

and a total bound *IG* wave potential in region III, $\Phi^{\mathrm{III},tot}_{bIG}$

$$\Phi^{\mathrm{III},tot}_{bIG} = \Phi^{\mathrm{III},D_1D_2}_{bIG} + \Phi^{\mathrm{III},R_1R_2}_{bIG} + \Phi^{\mathrm{III},D_1R_2}_{bIG} + \Phi^{\mathrm{III},D_2R_1}_{bIG}, \tag{2.13}$$

where the subscript *bIG* is for 'bound *IG* wave', while the superscript A_1A_2 etc. indicate which two carrier waves are interacting. Note that, in region I, no bound *IG* wave potential is generated due to the cross-interactions between the counter-propagating waves (i.e. between incident waves and the radiated/diffracted waves), see e.g. Agnon & Mei (1985, § 4). These potentials are shown in figure 2; they will be discussed in detail in § 4. Corresponding to these potentials, the total bound *IG* wave surface elevations in regions I and III are

$$\eta^{\mathrm{I},tot}_{bIG} = \eta^{\mathrm{I},A_1A_2}_{bIG} + \eta^{\mathrm{I},D_1D_2}_{bIG} + \eta^{\mathrm{I},R_1R_2}_{bIG} + \eta^{\mathrm{I},D_1R_2}_{bIG} + \eta^{\mathrm{I},D_2R_1}_{bIG}, \tag{2.14a}$$

$$\eta^{\mathrm{III},tot}_{bIG} = \eta^{\mathrm{III},D_1D_2}_{bIG} + \eta^{\mathrm{III},R_1R_2}_{bIG} + \eta^{\mathrm{III},D_1R_2}_{bIG} + \eta^{\mathrm{III},D_2R_1}_{bIG}. \tag{2.14b}$$

Figure 2 also shows free *IG* (subscript '*fIG*') wave potentials, *viz.* $\Phi^{\mathrm{I},M}_{fIG}$, $\Phi^{\mathrm{I},R}_{fIG}$, $\Phi^{\mathrm{III},M}_{fIG}$, $\Phi^{\mathrm{III},R}_{fIG}$, where the superscripts *R* and *M* represent radiated free *IG* waves and free *IG* waves required to satisfy the matching conditions. These, and the associated surface elevations, $\eta^{\mathrm{I},M}_{fIG}$, $\eta^{\mathrm{I},R}_{fIG}$, $\eta^{\mathrm{III},M}_{fIG}$, $\eta^{\mathrm{III},R}_{fIG}$, as well as the *IG* potentials in region II, $\Phi^{\mathrm{II},M}_{IG}$ and $\Phi^{\mathrm{II},R}_{IG}$, will be discussed in §§ 5 and 6.

The sum of free and bound *IG* surface elevations gives the total *IG* waves. Denote the total *IG* wave potential in regions I and III by $\Phi^{\mathrm{I},tot}_{IG}$ and $\Phi^{\mathrm{III},tot}_{IG}$, they are

$$\Phi^{\mathrm{I},tot}_{IG} = \Phi^{\mathrm{I},M}_{fIG} + \Phi^{\mathrm{I},R}_{fIG} + \Phi^{\mathrm{I},tot}_{bIG}; \quad \Phi^{\mathrm{III},tot}_{IG} = \Phi^{\mathrm{III},M}_{fIG} + \Phi^{\mathrm{III},R}_{fIG} + \Phi^{\mathrm{III},tot}_{bIG}, \tag{2.15a,b}$$

https://doi.org/10.1017/jfm.2025.10514 Published online by Cambridge University Press

$k_{0,1}$, $k_{0,2}$: wavenumbers of first-order waves.
ω_1, ω_2 or f_1, f_2: frequencies of incident carrier waves. $\omega_2 = 1.1\omega_1$ in this paper.
A_1, A_2: real amplitudes of incident carrier waves
$a_{0,1}$, $a_{0,1}$: complex amplitudes of diffracted waves in region I
$\mathfrak{a}_{0,1}$, $\mathfrak{a}_{0,2}$: complex amplitudes of radiated waves in region I
$b_{0,1}$, $b_{0,1}$: complex amplitudes of diffracted waves in region III
$\mathfrak{b}_{0,1}$, $\mathfrak{b}_{0,1}$: complex amplitudes of radiated waves in region III
η_1^{I,A_1}, η_2^{I,A_2}: surface elevations of incident ('approaching') waves (in region I only)
η_1^{I,D_1}, η_2^{I,D_2}: surface elevations of diffracted waves in region I
η_1^{I,R_1}, η_2^{I,R_2}: surface elevations of radiated waves in region I
$\eta_1^{\mathrm{III},D_1}$, $\eta_2^{\mathrm{III},D_2}$: surface elevations of diffracted waves in region III
$\eta_1^{\mathrm{III},R_1}$, $\eta_2^{\mathrm{III},R_2}$: surface elevations of radiated waves in region III

Table 1. A summary of quantities related to first-order waves mentioned in § 3.

which corresponds to the surface elevation: $\eta_{IG}^{\mathrm{I},tot}$ and $\eta_{IG}^{\mathrm{III},tot}$, their details are

$$\eta_{IG}^{\mathrm{I},tot} = \eta_{fIG}^{\mathrm{I},M} + \eta_{fIG}^{\mathrm{I},R} + \eta_{bIG}^{\mathrm{I},tot}; \quad \eta_{IG}^{\mathrm{III},tot} = \eta_{fIG}^{\mathrm{III},M} + \eta_{fIG}^{\mathrm{III},R} + \eta_{bIG}^{\mathrm{III},tot}. \tag{2.16a,b}$$

Our primary interest here is controlling the amplitude of $\eta_{IG}^{\mathrm{III},tot}$ by suitable 2-D heaving block.

3. Carrier waves modified by a 2-D heaving body

When the two linear carrier waves encounter the heaving block in figure 2, diffracted and radiated waves are generated. Both incident waves are discussed to familiarise the reader with the symbol system used throughout the paper. Parameters in this section are listed in table 1 for easier reference.

3.1. *Governing equations*

The governing equations and boundary conditions for the diffraction problem are (2.9) plus the following boundary condition on the floating body:

$$\frac{\partial \Phi_1}{\partial n} = 0\Big|_{\text{on } s_{1,2,3}}, \tag{3.1}$$

where n represents normal vectors of surfaces $s_{1,2,3}$ in figure 2. For the heaving radiation problem, the block's vertical velocity is

$$\dot{\xi}(\mathrm{t}) = -\mathrm{i}\omega A_h \mathrm{e}^{-\mathrm{i}\omega \mathrm{t}}, \tag{3.2}$$

where A_h is an unknown complex heaving amplitude, and ω is the angular frequency of the incident wave. To determine it, the following boundary condition on the bottom of the block is required, stating that the z-velocity of the flow equals the heaving velocity:

$$\frac{\partial \Phi_1}{\partial z} = -\mathrm{i}\omega A_h \mathrm{e}^{-\mathrm{i}\omega \mathrm{t}}\Big|_{\text{on the bottom of the block, } s_2}. \tag{3.3}$$

https://doi.org/10.1017/jfm.2025.10514 Published online by Cambridge University Press

3.2. *Incident waves*

Incident waves in figure 2 approach from the negative x-axis, satisfying (2.9) in region I. Sinusoidal surface profiles are well-known solutions (see Appendix B)

$$\eta^{\mathrm{I},A_1} = A_1\cos(k_{0,1}\mathfrak{x} - \omega_1\mathfrak{t}), \quad \eta^{\mathrm{I},A_2} = A_2\cos(k_{0,2}\mathfrak{x} - \omega_2\mathfrak{t}), \tag{3.4}$$

where the superscripts 'I, A_n' ($n = 1, 2$) denote incident waves 1 and 2 in region I (see figure 2 for region division). The letter 'I' denotes region I, and the letter 'A' denotes 'approaching' waves, a term used as an alternative for 'incident' waves, to avoid using the letter 'I' again in the superscripts. The real quantities A_n, $k_{0,n}$, ω_n, ($n = 1, 2$) are wave amplitudes, wavenumber and wave frequencies, respectively. Note that the subscript 0 in $k_{0,n}$ arises to ensure consistency with the notations in Appendix B. The values of $k_{0,n}$ satisfy the dispersion relations

$$\omega_1^2 = \mathrm{g}k_{0,1}\tanh k_{0,1}h, \quad \omega_2^2 = \mathrm{g}k_{0,2}\tanh k_{0,2}h. \tag{3.5}$$

The majority of examples in this paper assume that $\omega_2 = 1.1\omega_1$ (cf. Hossain *et al.* 2001; Sergiienko *et al.* 2024); other frequencie ratios are discussed briefly in § 9.2.

3.3. *Diffracted and radiated waves*

When waves given by (3.4) interact with the 2-D heaving block, diffracted and radiated wave fields are generated. The governing equations are (2.9), (3.1) and (3.3). Generally, the diffracted and radiated waves can be described by infinite sums of eigenfunctions involving progressive and evanescent modes. Evanescent modes are neglected because they decay rapidly away from the block and do not spawn *IG* waves (Agnon *et al.* 1988; Liu & Iskandarani 1991; Hermans 2010). Using the superscripts D_1, D_2 to denote diffracted waves related to incident carrier waves 1 and 2, using the superscripts R_1, R_2 to denote radiated waves 1 and 2 and using 'I' for waves in region I and 'III' for waves in region III, the progressive modes of the eight diffracted and radiated waves are

$$\eta^{\mathrm{I},D_n} = \left|a_{0,1}^-\right|\cos\left[-k_{0,n}(\mathfrak{x}-(-L)) - \omega_n\mathfrak{t} + \arg\left(a_{0,n}^-\right)\right], \quad n = 1, 2, \tag{3.6a}$$

$$\eta^{\mathrm{I},R_n} = \left|\mathfrak{a}_{0,n}^-\right|\cos\left[-k_{0,n}(\mathfrak{x}-(-L)) - \omega_n\mathfrak{t} + \arg\left(\mathfrak{a}_{0,n}^-\right)\right], \quad n = 1, 2, \tag{3.6b}$$

$$\eta^{\mathrm{III},D_n} = \left|b_{0,n}^+\right|\cos\left[k_{0,n}(\mathfrak{x}-L) - \omega_n\mathfrak{t} + \arg\left(b_{0,n}^+\right)\right], \quad n = 1, 2, \tag{3.6c}$$

$$\eta^{\mathrm{III},R_n} = \left|\mathfrak{b}_{0,n}^+\right|\cos\left[k_{0,n}(\mathfrak{x}-L) - \omega_n\mathfrak{t} + \arg\left(\mathfrak{b}_{0,n}^+\right)\right], \quad n = 1, 2, \tag{3.6d}$$

where $a_{0,1}^-$, $a_{0,2}^-$, $\mathfrak{a}_{0,1}^-$, $\mathfrak{a}_{0,2}^-$ are unknown coefficients for reflected waves in region I, and $b_{0,1}^+$, $b_{0,2}^+$, $\mathfrak{b}_{0,1}^+$, $\mathfrak{b}_{0,2}^+$ for transmitted waves in region III. These coefficients are solved in Appendices B and C. To this end, (2.10) and (2.11) are fully specified. All wave surface elevations in this paper are presented in real form, like (3.6). This is because surface elevations are inherently real quantities, and unlike flow potentials, they are final results that no longer participate in important calculations. Hence, a real presentation is suitable.

4. Bound infragravity waves around the heaving body

Due to nonlinearities in boundary conditions, the linear wave solutions, (3.4) and (3.6), interact and generate new waves including higher-frequency superharmonics (see e.g. figure 1*d*) not relevant to this study, and lower-frequency subharmonics (*IG* waves), which are of interest. As mentioned in § 2, to determine the *IG* wave potential, $O(\varepsilon^2)$ and $O(\varepsilon^3)$ analyses are needed. We neglect the well-documented details (Mei *et al.* 2005) and present

https://doi.org/10.1017/jfm.2025.10514 Published online by Cambridge University Press

results only: they are bound *IG* waves due to interactions between incident, diffracted and radiated carrier waves, and due to cross-interactions between radiated and diffracted carrier waves.

4.1. *Bound IG wave potentials due to interaction of incident carrier waves*

Use $\Phi_{bIG}^{\mathrm{I},A_1A_2}$ to denote the flow potential of the bound *IG* wave generated by the two incident carrier waves (3.4). The subscript '*bIG*' stands for 'bound *IG* waves', the superscript 'I' means that the bound *IG* wave is in region I and A_1A_2 indicates that it is generated by the interaction of two incident carrier waves A_1 and A_2 where, as before, *A* stands for 'approaching waves'. The potential is governed by the following equation (cf. (13.2.36) of Mei & Benmoussa 1984; Mei *et al.* 2005; and Liu & Iskandarani 1991):

$$\frac{\partial^2\Phi_{bIG}^{\mathrm{I},A_1A_2}}{\partial T^2}-\mathrm{g}h\frac{\partial^2\Phi_{bIG}^{\mathrm{I},A_1A_2}}{\partial X^2}=\mathrm{i}\left(\frac{\mathrm{g}^2k_Sk_L}{\omega_S}+\frac{\omega_S^2\omega_L}{2\sinh^2k_Sh}\right)\times\left[\mathrm{e}^{2\mathrm{i}(k_LX-\omega_LT)}-\mathrm{e}^{-2\mathrm{i}(k_LX-\omega_LT)}\right]A_1A_2, \tag{4.1}$$

where X and T are slow-varying spatial and temporal scales, k_S, ω_S, k_L and ω_L are defined as follows:

$$\omega_L=\left|\frac{\omega_1-\omega_2}{2}\right|,\quad \omega_S=\frac{\omega_1+\omega_2}{2},\quad k_L=\left|\frac{k_{0,1}-k_{0,2}}{2}\right|,\quad k_S=\frac{k_{0,1}+k_{0,2}}{2}. \tag{4.2}$$

Physically, the former two are the averaged wavenumber and angular frequency of the carrier waves. The subscript *S* stands for 'short waves', and *L* stands for 'long waves'. To obtain the wavenumber and frequency of the *IG* wave, one should multiply both k_L and ω_L by 2. This is because k_L and ω_L are defined in such a way in past studies (e.g. Mei *et al.* 2005); we follow the tradition.

Equation (4.1) contains a homogeneous part for $\Phi_{bIG}^{\mathrm{I},A_1A_2}$ on the left-hand side and an inhomogeneous forcing term proportional to the product of carrier waves' amplitudes, A_1A_2, on the right-hand side. The particular solution to (4.1) is

$$\Phi_{bIG}^{\mathrm{I},A_1A_2}=C_BA_1A_2\left[\mathrm{e}^{2\mathrm{i}(k_LX-\omega_LT)}-\mathrm{c.c.}\right], \tag{4.3}$$

where 'c.c.' stands for complex conjugate, and the coefficient C_B is defined as

$$C_B=\frac{\mathrm{i}}{\left(-4\omega_L^2+4\mathrm{g}hk_L^2\right)}\left(\frac{\mathrm{g}^2k_Sk_L}{\omega_S}+\frac{\omega_S^2\omega_L}{2\sinh^2k_Sh}\right). \tag{4.4}$$

Equation (4.3) is not a function of z, as (4.1) does not contain z.

4.2. *Bound IG wave potentials due to diffracted and radiated carrier waves*

The diffracted and radiated first-order waves expressed by (3.6) also generate bound *IG* wave potentials. The *IG* wave potentials due to interaction between diffracted waves in regions I and III are denoted by $\Phi_{bIG}^{\mathrm{I},D_1D_2}$ and $\Phi_{bIG}^{\mathrm{III},D_1D_2}$, respectively, while *IG* wave potentials due to interactions between radiated waves in regions I and III are denoted by $\Phi_{bIG}^{\mathrm{I},R_1R_2}$ and $\Phi_{bIG}^{\mathrm{III},R_1R_2}$. The bound *IG* wave potential arising from cross-interactions between diffracted and radiated carrier wave are $\Phi_{bIG}^{\mathrm{I},D_1R_1}$, $\Phi_{bIG}^{\mathrm{I},D_2R_1}$, $\Phi_{bIG}^{\mathrm{III},D_1R_2}$, $\Phi_{bIG}^{\mathrm{III},D_2R_1}$, $\Phi_{bIG}^{\mathrm{I},D_1R_2}$. These wave potentials are governed by equations similar to (4.1), and their details are given in Appendix D. It should be noted that there is no *IG* wave arising from interactions between waves of the same frequency; therefore, the following *IG* wave

https://doi.org/10.1017/jfm.2025.10514 Published online by Cambridge University Press

potentials do not exist: $\Phi_{bIG}^{\mathrm{I},D_1R_1}$, $\Phi_{bIG}^{\mathrm{III},D_1R_1}$, $\Phi_{bIG}^{\mathrm{I},D_2R_2}$, $\Phi_{bIG}^{\mathrm{III},D_2R_2}$. Moreover, as noted in § 2, no bound *IG* waves are generated by the interaction between incident waves and radiated/diffracted waves in region I. To this end, all elements in (2.12) and (2.13) are explained.

4.3. *Bound IG wave surface elevations*

The bound *IG* wave potentials each give rise to surface elevations. For example, the incident bound *IG* wave potential $\Phi_{bIG}^{\mathrm{I},A_1A_2}$ corresponds to the following surface elevation (cf. 2.9):

$$-\frac{1}{\mathrm{g}}\frac{\partial \Phi_{bIG}^{\mathrm{I},A_1A_2}}{\partial T} = 2C_1A_1A_2\cos\left[2\left(k_LX-\omega_LT\right)\right], \tag{4.5}$$

in which

$$C_1 = -\frac{\omega_L}{2\mathrm{g}k_L^2\left(-C_g^2+\mathrm{g}h\right)}\left(\frac{\mathrm{g}^2k_Sk_L}{\omega_S}+\frac{\omega_S^2\omega_L}{2\sinh^2 k_Sh}\right). \tag{4.6}$$

The surface elevation expressed by (4.5) is incomplete; it needs to be amended by another comparably small *IG* wave, due to $O(\varepsilon^2)$ self-interactions of carrier wave components, cf. (13.2.33) of Mei *et al.* (2005), to yield the complete surface elevation for the incident bound *IG* wave $\eta_{bIG}^{\mathrm{I},A_1A_2}$

$$\eta_{bIG}^{\mathrm{I},A_1A_2} = 2\left(C_1+C_2\right)A_1A_2\cos\left[2\left(k_LX-\omega_LT\right)\right], \tag{4.7}$$

where C_2 is the amplitude of the other *IG* wave

$$C_2 = -\frac{k_S}{2\sinh 2k_Sh}. \tag{4.8}$$

Similarly, bound *IG* waves due to interactions between diffracted waves in regions I and III are denoted by $\eta_{bIG}^{\mathrm{I},D_1D_2}$ and $\eta_{bIG}^{\mathrm{III},D_1D_2}$, respectively, while bound *IG* waves generated by interactions between radiated waves in regions I and III are denoted by $\eta_{bIG}^{\mathrm{I},R_1R_2}$ and $\eta_{bIG}^{\mathrm{III},R_1R_2}$. Bound *IG* waves due to cross-interactions between diffracted and radiated carrier waves are $\eta_{bIG}^{\mathrm{I},D_1R_1}$, $\eta_{bIG}^{\mathrm{I},D_2R_1}$, $\eta_{bIG}^{\mathrm{III},D_1R_2}$, $\eta_{bIG}^{\mathrm{III},D_2R_1}$, $\eta_{bIG}^{\mathrm{I},D_1R_2}$. Their details are given in Appendix E. These waves contribute to (2.14).

5. Free infragravity waves to satisfy matching conditions

5.1. *Free IG wave potentials and surface elevations*

The total bound *IG* wave potentials (2.12 and 2.13) are generally discontinuous across the block. To rectify this, free *IG* wave potentials in regions I and III, denoted by $\Phi_{fIG}^{\mathrm{I},M}$ and $\Phi_{fIG}^{\mathrm{III},M}$ (subscript f*IG* for free *IG* waves), are introduced. In region II, the second-order potential is $\Phi_{IG}^{\mathrm{II},M}$ (the subscript is '*IG*' but not '*fIG*'; it corresponds to neither free nor bound waves). Among the unknowns, $\Phi_{fIG}^{\mathrm{I},M}$ and $\Phi_{fIG}^{\mathrm{III},M}$ should satisfy the homogeneous version of (4.1), hence

$$\Phi_{fIG}^{\mathrm{I},M} = D^{\mathrm{I}}\mathrm{e}^{-2\mathrm{i}\frac{\omega_L}{\sqrt{\mathrm{g}h}}X}\mathrm{e}^{-2\mathrm{i}\omega_LT}+\mathrm{c.c.},\quad \Phi_{fIG}^{\mathrm{III},M} = D^{\mathrm{III}}\mathrm{e}^{2\mathrm{i}\frac{\omega_L}{\sqrt{\mathrm{g}h}}X}\mathrm{e}^{-2\mathrm{i}\omega_LT}+\mathrm{c.c.} \tag{5.1}$$

https://doi.org/10.1017/jfm.2025.10514 Published online by Cambridge University Press

In (5.1), there are four unknown coefficients: D^{I}, D^{III} and their complex conjugates, $\overline{D^{\mathrm{I}}}$, $\overline{D^{\mathrm{III}}}$. The remaining potential $\Phi_{IG}^{\mathrm{II},M}$ should satisfy the Laplace equation and the boundary conditions on the block's bottom s_2 (see figure 2) and on the sea bottom. The following solution can be used (cf. (B6) in Appendix B, also see Hossain *et al.* 2001):

$$\Phi_{IG}^{\mathrm{II},M} = (\mathcal{A}_1 X + \mathcal{A}_2)\mathrm{e}^{-2\mathrm{i}\omega_L T} + \text{c.c.}, \tag{5.2}$$

which contains four more unknown coefficients: $\mathcal{A}_1$, $\mathcal{A}_2$ and their complex conjugates $\overline{\mathcal{A}_1}$ and $\overline{\mathcal{A}_2}$, increasing the number of unknowns to eight, requiring eight equations. They are determined by the following four matching conditions, which require that the total *IG* wave potential and flux are continuous at both the bow ($X = -L$) and the stern ($X = L$) of the heaving block (Agnon *et al.* 1988; Wu & Liu 1990; Liu & Iskandarani 1991; Hossain *et al.* 2001; Li *et al.* 2021)

$$\Phi_{bIG}^{\mathrm{I},tot} + \Phi_{fIG}^{\mathrm{I},M}\Big|_{X=-L} = \Phi_{IG}^{\mathrm{II},M}\Big|_{X=-L}, \tag{5.3}$$

$$\Phi_{IG}^{\mathrm{II},M}\Big|_{X=L} = \Phi_{bIG}^{\mathrm{III},tot} + \Phi_{fIG}^{\mathrm{III},M}\Big|_{X=L}, \tag{5.4}$$

$$\frac{\Phi_{bIG}^{\mathrm{I},tot}}{\partial X} + \frac{\Phi_{fIG}^{\mathrm{I},M}}{\partial X}\Big|_{X=-L} = \frac{\Phi_{IG}^{\mathrm{II},M}}{\partial X}\Big|_{X=-L}, \tag{5.5}$$

$$\frac{\Phi_{IG}^{\mathrm{II},M}}{\partial X}\Big|_{X=L} = \frac{\Phi_{bIG}^{\mathrm{III},tot}}{\partial X} + \frac{\Phi_{fIG}^{\mathrm{III},M}}{\partial X}\Big|_{X=L}. \tag{5.6}$$

Substituting the known quantities $\Phi_{bIG}^{\mathrm{I},tot}$ and $\Phi_{bIG}^{\mathrm{III},tot}$ into (5.3–5.6) and collocating like time harmonics yields eight equations, see Appendix F. Solving the equations determines the unknown potentials, then the surface elevations of the free *IG* waves $\eta_{fIG}^{\mathrm{I},M}$ and $\eta_{fIG}^{\mathrm{III},M}$ can be calculated by

$$\eta_{fIG}^{\mathrm{I},M} = -\frac{1}{\mathrm{g}}\frac{\partial \Phi_{fIG}^{\mathrm{I},M}}{\partial T},\ X < -L; \quad \eta_{fIG}^{\mathrm{III},M} = -\frac{1}{\mathrm{g}}\frac{\partial \Phi_{fIG}^{\mathrm{III},M}}{\partial T},\ X > L. \tag{5.7a,b}$$

The free *IG* waves, (5.1) and (5.2), as well as the matching conditions (5.3–5.6), are approximations, as they do not satisfy the governing equations and boundary conditions on the heaving block exactly; moreover, the free *IG* waves are assumed to be shallow water waves (see e.g. Li *et al.* 2021, § 2.6.3).

5.2. *A note on total IG wave amplitude modulation*

The free *IG* wave's phase speed $\sqrt{\mathrm{g}h}$ is generally faster than the bound *IG* wave's phase speed (the group velocity)

$$C_{bIG} = \frac{\omega_L}{k_L} = C_g. \tag{5.8}$$

As such, when a localised wave packet interacts with an obstacle (e.g. Li *et al.* 2021), the free *IG* wave will overtake the bound *IG* wave, so that the total amplitude of the *IG* wave is location-dependent. Such an amplitude variation of second-order waves was also observed by Massel (1983). However, these previous studies did not systematically consider *IG* wave amplitude modulation from a wave reduction/coastal protection point of view using heaving bodies.

https://doi.org/10.1017/jfm.2025.10514 Published online by Cambridge University Press

6. Free infragravity waves radiated by second-order heaving

The previous section reveals that a second-order wave potential $\Phi_{IG}^{\mathrm{II},M}$ exists in region II. This creates a force that drives the block to a 'slow' heaving motion $\xi_{IG}(T)$ at the frequency of *IG* waves. Similar to the 'fast' heaving radiation problem where the carrier wave potential in region II excites the block into fast heaving (3.2), this slow motion generates a wave potential $\Phi_{IG}^{\mathrm{II},R}$ and associated free *IG* waves. Details are presented below where $\xi_{IG}(T)$ and $\Phi_{IG}^{\mathrm{II},R}$ are determined.

6.1. *Slow heaving*

The slow heaving motion due to the second-order potential $\Phi_{IG}^{\mathrm{II},M}$ (5.2) is characterised by its amplitude denoted by A_h^{IG} and its complex conjugate $\overline{A_h^{IG}}$. Assuming that slow heaving is a periodic function of time, then its displacement $\xi_{IG}(T)$ can be expressed as

$$\xi_{IG}(T) = A_h^{IG}\mathrm{e}^{-2\mathrm{i}\omega_L T} + \mathrm{c.c.} \tag{6.1}$$

Equation (6.1) implies the following slow heaving velocity and acceleration:

$$\dot{\xi}_{IG}(T) = -2\mathrm{i}\omega_L A_h^{IG}\mathrm{e}^{-2\mathrm{i}\omega_L T} + \mathrm{c.c.}, \quad \ddot{\xi}_{IG}(T) = -4\omega_L^2 A_h^{IG}\mathrm{e}^{-2\mathrm{i}\omega_L T} + \mathrm{c.c.}. \tag{6.2}$$

The unknown amplitudes A_h^{IG} and $\overline{A_h^{IG}}$ are decided by a force balance equation. The excitation force in the equation is calculated by

$$F_{IG}^{D} = \int_{-L}^{L} -\rho\frac{\partial\Phi_{IG}^{\mathrm{II},M}}{\partial T}\bigg|_{z=-d}\mathrm{d}X = 4\mathrm{i}\rho\mathrm{g}\omega_L\left(\mathcal{A}_2\mathrm{e}^{-2\mathrm{i}\omega_L T} - \overline{\mathcal{A}_2}\mathrm{e}^{2\mathrm{i}\omega_L T}\right). \tag{6.3}$$

For a block section with unit width, the restoring force is calculated as $F^S = \rho\mathrm{g}A_{wp}\xi_{IG}$, where the waterplane area $A_{wp} = 2L$. The inertia force F^M is calculated by $m\ddot{\xi}_{IG}$, where the mass m equals $2L\rho d$ for unit width. Finally, the radiation force F^R equals $-\ddot{\xi}m_a - \dot{\xi}R$, where the frequency-dependent added mass m_a and radiation damping R are evaluated at the frequency of the *IG* wave, $2\omega_L$. The analytical details of m_a and R are derived in Appendix C.2.

Balancing all forces by $F^M + F^S = F_{IG}^D + F^R$ and collecting different harmonics leads to two equations. Solving them yields A_h^{IG} and $\overline{A_h^{IG}}$

$$A_h^{IG} = \frac{2\mathrm{i}\rho\omega_L\mathcal{A}_2}{-2\omega_L^2(2L\rho d + m_a) - \mathrm{i}\omega_L R + \rho\mathrm{g}L}, \quad \overline{A_h^{IG}} = \frac{-2\mathrm{i}\rho\omega_L\overline{\mathcal{A}_2}}{-2\omega_L^2(2L\rho d + m_a) + \mathrm{i}\omega_L R + \rho\mathrm{g}L}. \tag{6.4}$$

6.2. *Radiated free IG wave potentials*

Once the slow heaving amplitudes A_h^{IG} and $\overline{A_h^{IG}}$ are determined, the slow heaving flow potential can be determined. Denote the flow potential by $\Phi_{IG}^{\mathrm{II},R}$ (the superscript R stands for radiation); similar to $\Phi_{IG}^{\mathrm{II},M}$ discussed in the last section, it should also satisfy the Laplace equation and the boundary conditions on s_2 and on the sea bottom, cf. (2.9) and (3.1). In addition, it should satisfy the following boundary condition stating that the z-derivative of $\Phi_{IG}^{\mathrm{II},R}$ gives heaving velocity on the bottom of the block, s_2:

$$\frac{\partial\Phi_{IG}^{\mathrm{II},R}}{\partial z} = \dot{\xi}_{IG}(T)\bigg|_{s_2}. \tag{6.5}$$

https://doi.org/10.1017/jfm.2025.10514 Published online by Cambridge University Press

A solution is (cf. C4)

$$\Phi_{IG}^{\mathrm{II},R} = (\mathcal{B}_1 x + \mathcal{B}_2)\,\mathrm{e}^{-2\mathrm{i}\omega_L T} + A_h^{IG}\frac{(z+h)^2 - x^2}{2(h-d)}\mathrm{e}^{-2\mathrm{i}\omega_L T} + \mathrm{c.c.}, \tag{6.6}$$

which contains four unknowns, $\mathcal{B}_1$, $\mathcal{B}_2$ and their complex conjugates $\overline{\mathcal{B}_1}$, $\overline{\mathcal{B}_2}$. The potential $\Phi_{IG}^{\mathrm{II},R}$ generates radiated waves in regions I and III, and it is envisaged that these waves assume the same form as the free *IG* waves discussed before. Denoting these radiated free *IG* wave potentials by $\Phi_{fIG}^{\mathrm{I},R}$ and $\Phi_{fIG}^{\mathrm{III},R}$, their details are

$$\Phi_{fIG}^{\mathrm{I},R} = \mathfrak{D}^{\mathrm{I}}\mathrm{e}^{-2\mathrm{i}\frac{\omega_L}{\sqrt{gh}}X}\mathrm{e}^{-2\mathrm{i}\omega_L T} + \mathrm{c.c.} \quad \Phi_{fIG}^{\mathrm{III},R} = \mathfrak{D}^{\mathrm{III}}\mathrm{e}^{2\mathrm{i}\frac{\omega_L}{\sqrt{gh}}X}\mathrm{e}^{-2\mathrm{i}\omega_L T} + \mathrm{c.c.} \tag{6.7}$$

Equation (6.7) contains four more unknown coefficients, $\mathfrak{D}^{\mathrm{I}}$, $\mathfrak{D}^{\mathrm{III}}$ and their complex conjugates $\overline{\mathfrak{D}^{\mathrm{I}}}$ and $\overline{\mathfrak{D}^{\mathrm{III}}}$. The unknowns are determined by the following four matching conditions stating that the vertical integrals of the potentials and their fluxes in (6.6) and (6.7) are continuous at the bow ($X = -L$) and the stern ($X = L$) of the heaving body:

$$\int_{-h}^{0}\Phi_{fIG}^{\mathrm{I},R}\mathrm{d}z = \int_{-h}^{-d}\Phi_{IG}^{\mathrm{II},R}\mathrm{d}z\Big|_{X=-L}, \tag{6.8}$$

$$\int_{-h}^{-d}\Phi_{IG}^{\mathrm{II},R}\mathrm{d}z = \int_{-h}^{0}\Phi_{fIG}^{\mathrm{III},R}\mathrm{d}z\Big|_{X=L}, \tag{6.9}$$

$$\int_{-h}^{0}\frac{\partial\Phi_{fIG}^{\mathrm{I},R}}{\partial X}\mathrm{d}z = \int_{-h}^{-d}\frac{\partial\Phi_{IG}^{\mathrm{II},R}}{\partial X}\mathrm{d}z\Big|_{X-L}, \tag{6.10}$$

$$\int_{-h}^{0}\frac{\partial\Phi_{IG}^{\mathrm{II},R}}{\partial X}\mathrm{d}z = \int_{-h}^{-d}\frac{\partial\Phi_{fIG}^{\mathrm{III},R}}{\partial X}\mathrm{d}z\Big|_{X=-L}. \tag{6.11}$$

Substituting the contents of $\Phi_{fIG}^{\mathrm{I},R}$, $\Phi_{IG}^{\mathrm{II},R}$ and $\Phi_{fIG}^{\mathrm{III},R}$ into the above matching conditions and collecting like terms, one obtains eight equations determining all eight unknowns $\mathcal{B}_1$, $\mathcal{B}_2$, $\overline{\mathcal{B}_1}$, $\overline{\mathcal{B}_2}$, $\mathfrak{D}^{\mathrm{I}}$, $\mathfrak{D}^{\mathrm{III}}$, $\overline{\mathfrak{D}^{\mathrm{I}}}$ and $\overline{\mathfrak{D}^{\mathrm{III}}}$.

The radiated free *IG* waves can now be calculated by (cf. 5.7)

$$\eta_{fIG}^{\mathrm{I},R} = -\frac{1}{\mathrm{g}}\frac{\partial\Phi_{fIG}^{\mathrm{I},R}}{\partial T},\ X < -L; \quad \eta_{fIG}^{\mathrm{III},R} = -\frac{1}{\mathrm{g}}\frac{\partial\Phi_{fIG}^{\mathrm{III},R}}{\partial T},\ X > L. \tag{6.12a,b}$$

To this end, all unknowns in (2.16) are determined.

7. Some results for diffraction-only 2-D blocks

Results of the total *IG* wave field, (2.16), will be presented for stationary blocks (diffraction-only) first. The results are obtained by removing all radiation-related quantities. Only *IG* waves in region III will be presented, because region III is in the lee of the block, and from a coastal protection point of view, this is the region of interest. There, the total *IG* waves involve both bound and free types according to (2.16). Both types, as well as the total *IG* waves, will be presented.

7.1. *An example*

We start by providing in figure 3 an example ($L = 0.1h$, $d = 0.5h$, $k_{0,1}h = 1.20$, $A_1 = A_2 = 0.04$ m, $h = 1$ m) to illustrate carrier and *IG* waves around a stationary block.

https://doi.org/10.1017/jfm.2025.10514 Published online by Cambridge University Press

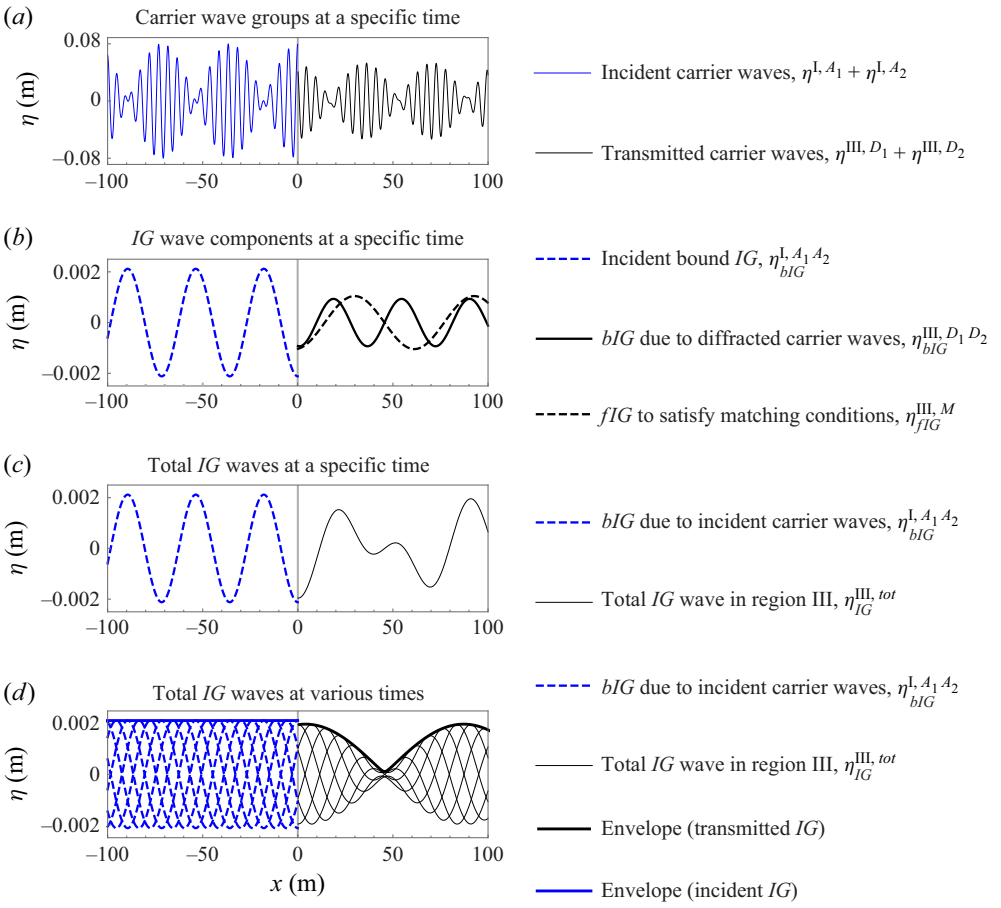


Figure 3. An illustration of wave components around a 2-D stationary block (diffraction only). The case is taken from the red curves of the second column of figure 5 where $L/h=0.1$, $d/h=0.5$. The value of $k_{0,1}h$ is set to 1.20. The figures show surface elevation η for: (*a*) carrier waves; (*b*) incident and transmitted *IG* waves; (*c*) total *IG* waves at $t=0$; (*d*) total *IG* waves evaluated at various times, revealing the modulated amplitude envelope. In all plots, b*IG* means bound *IG* waves, and f*IG* means free *IG* waves. See § 7.1.

Panel (*a*) shows carrier waves; bound and free *IG* waves are given in panel (*b*). The total transmitted *IG* wave is given in panel (*c*) for $T=0$, while in panel (*d*), total *IG* waves are evaluated at six different times, superimposed to reveal an amplitude envelope. Panel (*d*) also shows that the minimum transmitted total *IG* wave amplitude is near zero, but the maximum is almost one. The reason for such an amplitude modulation (cf. § 5.2) can be understood in view of panel (*b*), where the spatial wavelength of the transmitted free *IG* waves is almost twice the bound *IG* waves, so that when they superimpose, peaks and troughs in the total *IG* wave amplitude are created. In this case, if reducing total *IG* Waves is the goal, then the optimal location is approximately 50 m in the lee of the block.

7.2. *Systematic calculation of more cases*

Consider 2-D blocks specified by combinations of $L=0.01h$, $0.1h$, $1.0h$, $1.5h$, $2.0h$ and $d=0.1h$, $0.3h$, $0.5h$. All blocks are evaluated for wave conditions up to $k_{0,1}h=2$. The two carrier waves satisfy $f_2=1.1f_1$. To ensure the smallness of the blocks compared with

https://doi.org/10.1017/jfm.2025.10514 Published online by Cambridge University Press

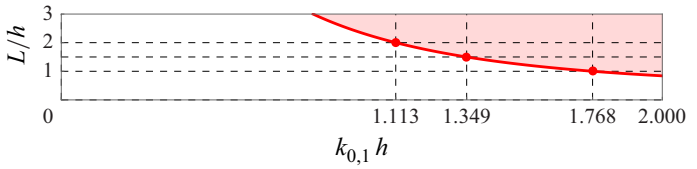


Figure 4. Validity range. For a given value of L/h, when the value of $k_{0,1}h$ is located to the right of the red curve (i.e. in the light region), then the inequality (7.1) fails. This diagram is calculated with $\omega_2 = 1.1\omega_1$ and $h = 1$ m. Gridlines are added to mark three points on the red curve corresponding to $L/h = 1$, 1.5 and 2. For details, see § 7.2.

the *IG* waves, it is required that

$$2L < \frac{2\lambda_g}{20}, \tag{7.1}$$

where $2L$ gives the total length of the block, $\lambda_g = 2\pi/(2k_L)$ is the length of the carrier wave group (so that the *IG* wave length is $2\lambda_g$). For blocks with $L = 0.01h$ and $0.1h$, the inequality (7.1) is always satisfied in the range $k_{0,1}h \in [0, 2]$. However, for blocks with $L = 1.0h$, $k_{0,1}h$ should be smaller than 1.768, for $L = 1.5h$, $k_{0,1}h$ should be smaller than 1.349 and when $L = 2.0h$, $k_{0,1}h$ should be less than 1.113. The $k_{0,1}h$ limits for other values of L/h are given in figure 4.

The transmission coefficient of carrier waves is discussed first. It is defined as

$$\text{transmission coefficient} = \frac{\text{amplitude of the transmitted carrier wave}}{\text{amplitude of the incident carrier wave}}. \tag{7.2}$$

The first row of figure 5 presents the transmission coefficient of the first carrier wave (with wavenumber $k_{0,1}$). The transmission of the second carrier wave (with wavenumber $k_{0,2}$) will follow the same trend, so it is omitted. A general observation from the first row of figure 5 is that the carrier waves are attenuated as L and d increase, meaning larger-sized blocks are more effective in reflecting the incident carrier waves.

The second row of figure 5 shows the normalised amplitude of total bound *IG* waves, as the ratio between the total bound *IG* wave amplitude in region III ($|\eta_{bIG}^{\mathrm{III},tot}|$) and the incident bound *IG* wave amplitude in region I ($|\eta_{bIG}^{\mathrm{I},A}|$). Similarly to the carrier wave's transmission coefficient, it reduces as L and d increase. The light red regions in figure 5 highlight the regimes where the inequality (7.1) is not respected, so caution should be exercised when interpreting the results in these red regions. In the light grey regions where $k_{0,1}h < 0.15$, no *IG* wave results are shown, because for the examples considered here (which assume that the water depth $h = 1$ m to be relevant to laboratory conditions), the *IG* wavelength is too long to be realistic when $k_{0,1}h < 0.15$.

The third row of figure 5 shows free *IG* waves in the form of the ratio between the total free *IG* wave amplitude in region III ($|\eta_{fIG}^{\mathrm{III},tot}|$) and the incident bound *IG* wave amplitude. The free *IG* wave increases as L and d increase, suggesting that reducing bound *IG* waves incurs a cost: the release of free *IG* waves. Note that in panels (*n*) and (*o*) of figure 5, the free *IG* wave can be noticeably larger than 1. Caution should be exercised when interpreting these results, as they occur in the light red regions where the condition (7.1) is not satisfied.

Adding up the bound and free waves in region III, one obtains the last row of figure 5, showing the total *IG* wave amplitude (i.e. $|\eta_{IG}^{\mathrm{III},tot}|$) normalised by the incident *IG* wave. Due to the reasons mentioned in § 5.2, $|\eta_{IG}^{\mathrm{III},tot}|$ is modulated: it depends not only on $k_{0,1}$, L, d, but also on the location x. For this reason, an upper bound (dashed lines) and a

https://doi.org/10.1017/jfm.2025.10514 Published online by Cambridge University Press

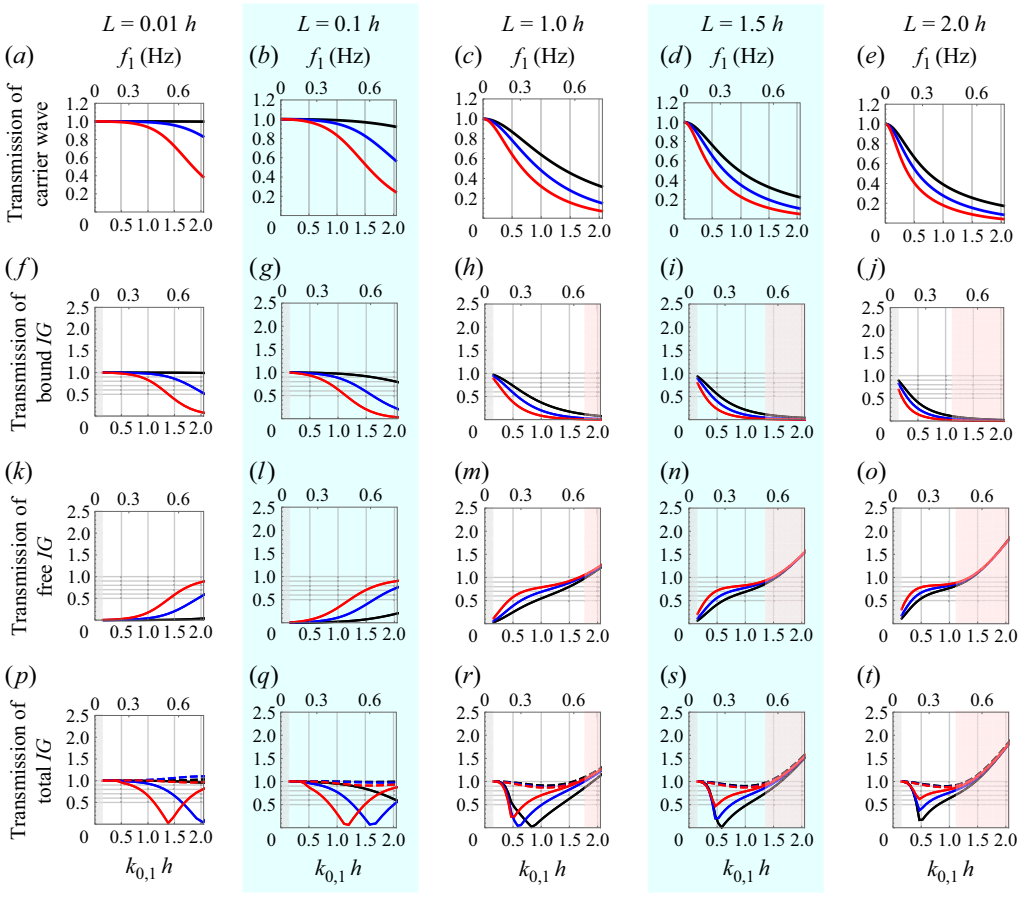


Figure 5. Wave modification due to stationary 2-D blocks. Five columns correspond to different L; see the legends at the top of each column. Light blue shades are added as visual guides to distinguish different columns. The four rows are: row 1, transmission coefficient for monochromatic waves with non-dimensional wavenumber $k_{0,1}h$. Row 2: the total bound *IG* wave amplitude in region III normalised by the incident bound *IG* wave amplitude. Row 3: similar to row 2 but for normalised free *IG* wave amplitude. Row 4: for total *IG* wave amplitude. In all plots, black, blue and red curves correspond to $d = 0.10h$, $0.30h$ and $0.50h$. In row 4, dashed and solid curves are the maximum and minimum amplitudes, respectively. In the red shades of plots (*n*, *o*, *s*, *t*, *x*, *y*), the condition (7.1) is not met, and the results may be invalid. In the light grey shades, $k_{0,1}h < 0.15$, and no results are presented. In all cases, the two carrier wave frequencies satisfy $f_2 = 1.1\,f_1$. These results are relevant to § 7.

lower bound (solid lines) exist when evaluating the total *IG* wave amplitude. It is clear that although the lower bound can be as small as zero (the *IG* wave is wholly eliminated), the upper bound is usually close to one (the *IG* wave amplitude is comparable to the incident *IG* wave).

7.3. *A summary: diffraction-only results*

This section reveals that when reducing the total *IG* waves is the goal, the best a diffraction-only block can do is the location-dependent reduction exemplified by figure 4(*d*): at some locations, the total *IG* wave amplitude is always near zero for all times, while at some other locations, the total *IG* wave is not reduced. This is due to the superposition of free and bound *IG* waves. Such a location-dependent reduction can be achieved by small-sized blocks (e.g. $L = 0.1h$) as well as larger blocks. The larger blocks have a stronger impact on

https://doi.org/10.1017/jfm.2025.10514 Published online by Cambridge University Press

lower values of $k_{0,1}h$ while the reverse is true for the small-sized blocks. If bound and free *IG* waves are shown separately, figure 5 shows that, when bound *IG* waves are small, free *IG* waves are non-small, *vice versa*. This aspect concurs with Liu & Iskandarani (1991).

8. Some results for heaving 2-D blocks

This section allows the blocks to heave. Heaving redistributes the energy of the incident wave field not only via diffraction but also via radiation; accordingly, the results will differ from the diffraction-only cases.

8.1. *An example*

An example is provided to demonstrate that the total *IG* waves can be reduced everywhere in the lee of a block. Consider a block with $d = 0.5h$, $L = 2.0h$. Set $k_{0,1}h = 0.95$, $A_1 = A_2 = 0.04$ m. The wave elevations around the block are presented in figure 6. Incident and transmitted carrier wave groups are given in panel (*a*). The *IG* waves bound to these wave groups are given in panel (*b*), which also shows bound *IG* waves due to cross-interaction between radiated and diffracted carrier waves, as well as free *IG* waves. The total *IG* waves are given in panel (*c*), evaluated at a specific time ($T = 0$). Evaluating the waves at more values of T and combining the plots, one obtains figure 6(*d*). The spatial amplitude modulation (cf. § 5.2) of the transmitted total *IG* waves is again observed. Despite the modulation, at all $x > L$ locations, the total *IG* waves are reduced everywhere.

8.2. *Systematic calculation of more cases*

Figure 7 shows results for heaving blocks. The transmission of the carrier waves is presented in the first row. Troughs of the transmission curves are related to the peaks of the heaving response amplitude operator (RAO) curves in the second row: when the values of $k_{0,1}h$ are to the right of the values of RAO peaks, the transmission coefficient quickly reduces (cf. Cui *et al.* 2023). The RAO peaks correspond to linear resonance; their locations are decided by both d and L: as d and L increase, they move to lower values of $k_{0,1}h$. The transmission of total bound *IG* waves is given by the third row of figure 7; their shapes are similar to the first row. These curves can be above unity, e.g. panels (*m*), (*n*), (*o*). The reason for this is given in Appendix G. The fourth row of figure 7 presents the amplitude of total free *IG* waves. Unlike the stationary blocks, the total free *IG* waves do not increase monotonically. The curves now have peaks and troughs, and the troughs can reach near-zero values, because the total free *IG* waves are the sum of induced free *IG* wave $\eta_{fIG}^{\mathrm{III},M}$ (5.7) and the radiated free *IG* wave $\eta_{fIG}^{\mathrm{III},R}$ (6.12); the two waves can interact destructively. The last row of figure 7 shows total *IG* wave (2.16). Like the diffraction-only case, the total *IG* wave amplitude has upper (dashed lines) and lower bounds. Unlike the diffraction-only case, where the upper bound is usually close to or above one, now the upper bounds can be noticeably lower than one, meaning the total *IG* waves can be reduced everywhere in the lee of the block. For the cases studied, these cases usually occur when $d = 0.5h$, and when $k_{0,1}h$ is greater or smaller than the RAO peaks, indicating that avoiding linear resonance leads to reduction of *IG* waves. The relationship between *IG* wave and RAO peaks is studied in more detail in the following subsection.

8.3. *Relating linear resonance (RAO peaks) to IG wave modification*

The previous subsection mentioned that for deeper-draught blocks ($d = 0.5h$), when $k_{0,1}h$ is located to either side of the RAO peak curve, the maximum total *IG* wave amplitude can be reduced, establishing a link between RAO curves (resulting from linear analysis)

https://doi.org/10.1017/jfm.2025.10514 Published online by Cambridge University Press

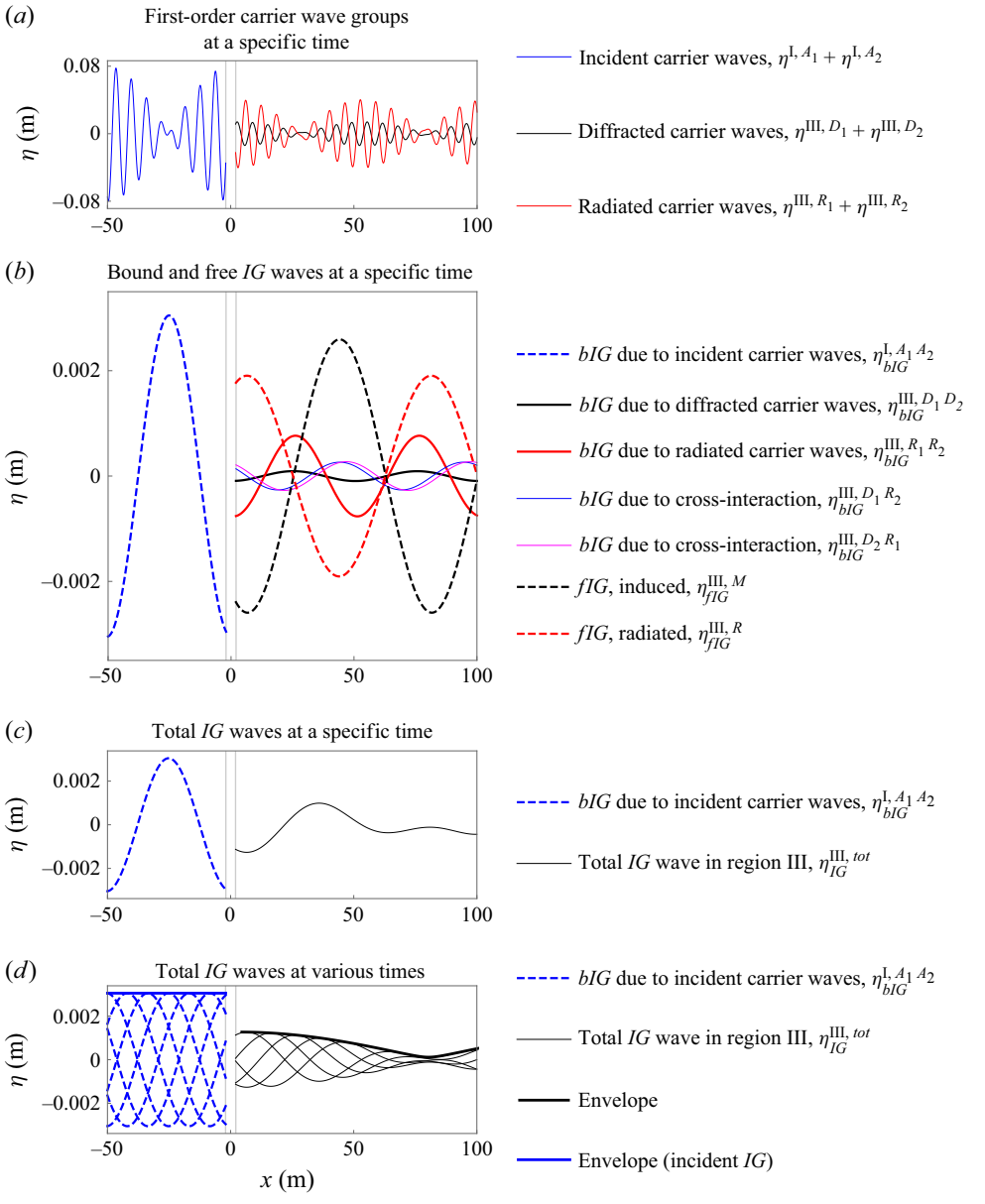


Figure 6. An illustration of wave components around a heaving 2-D block ($L=2h$, $d=0.5h$ where $h=1$ m, $k_{0,1}h=0.95$). These correspond to a case on the red curves in the fifth column of figure 7. Surface elevation η for: (*a*) first-order carrier waves; (*b*) incident and transmitted bound and free *IG* waves; (*c*) the total *IG* waves; (*d*) similar to (*c*) but evaluated at various times, illustrating the modulated amplitude envelope in region III. In all plots, b*IG* means bound *IG* waves, and f*IG* means free *IG* waves.

and *IG* waves (nonlinearly generated). This subsection studies this observation further, by overlapping locations of RAO peaks with *IG* wave results. To identify the trend clearly, L is now allowed to vary continuously, and the upper limit of L/h is increased from 2 to 3. The results are plotted in figure 8 in the form of heat maps, for the total free *IG* waves (row 1) and the maximum total *IG* waves (row 2). These quantities are related to row 4 of figure 7 and the dashed curves in row 5 of figure 7, respectively.

https://doi.org/10.1017/jfm.2025.10514 Published online by Cambridge University Press

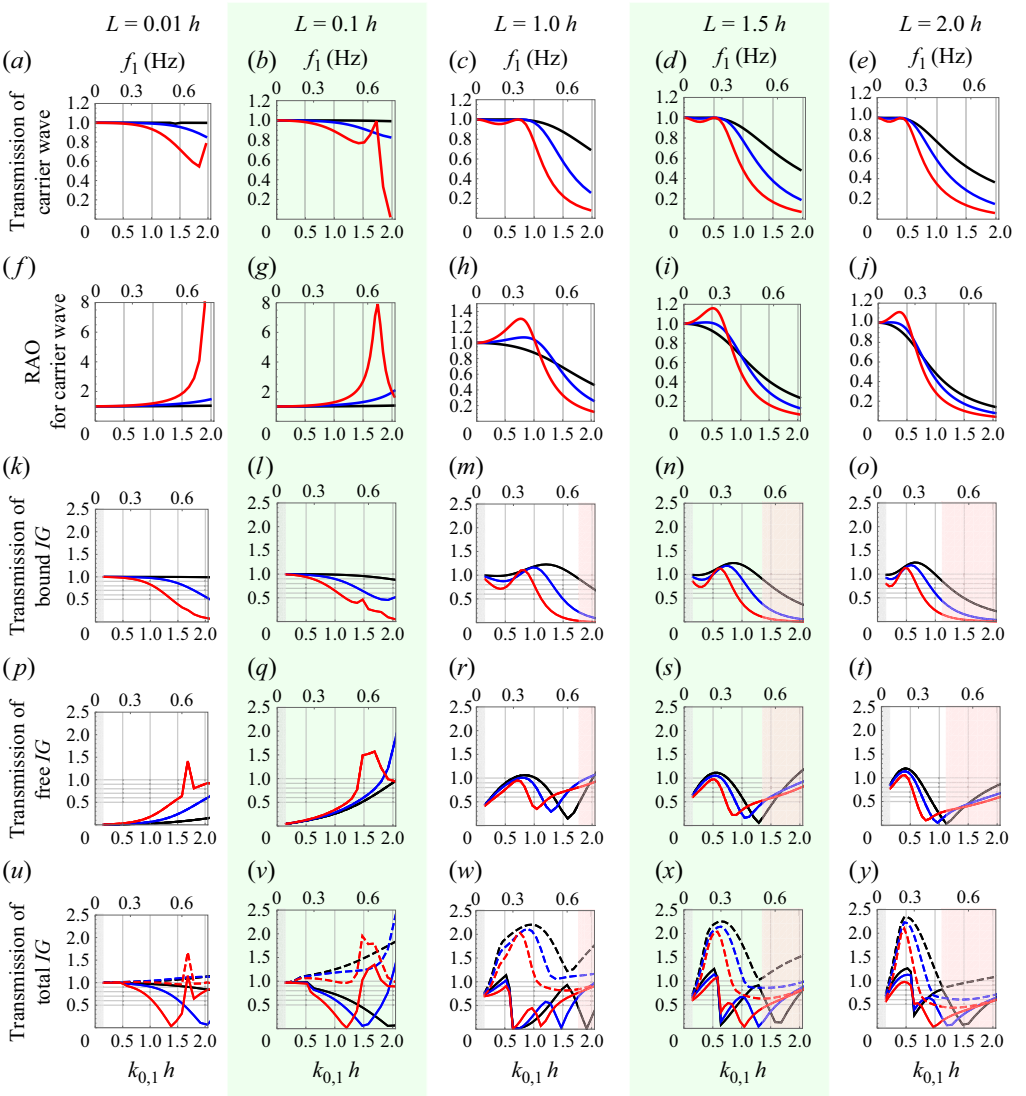


Figure 7. Wave modification due to heaving 2-D blocks. Five columns correspond to different L; see the legends at the top of each column. Light green shades are added to columns 2 and 4 as visual guides to distinguish different columns. Rows 1 and 2: transmission coefficient and RAO for monochromatic waves with non-dimensional wavenumber $k_{0,1}h$. Row 3: the total bound *IG* wave amplitude in region III normalised by the incident bound *IG* wave amplitude. Row 4: similar to row 3, but for total free *IG* wave amplitude. Row 5: similar to row 3, but for total *IG* wave amplitude. Black, blue and red curves correspond to $d = 0.10h$, $0.30h$ and $0.50h$. In row 5, dashed and solid curves are the maximum and minimum *IG* wave amplitudes, respectively. In all cases, the two carrier wave frequencies satisfy $f_2 = 1.1\,f_1$. In the red shades of plots (n, o, s, t, x, y), the condition (7.1) is not met, and the results may not be valid. In grey shades, $k_{0,1}h < 0.15$, results for *IG* waves are not presented. This figure is relevant to § 8.

The first row of figure 8 shows that, as d increases, the RAO peak curve (white curve) relocates to largely coincide with a red-coloured 'ridge' on the heat map where total free *IG* waves assume relatively large amplitudes. To both sides of the 'ridge', the free *IG* wave amplitudes decrease as the colour turns towards blue. The same conclusion applies to the second row of figure 8, where maximum total *IG* waves are shown. These conclusions do

https://doi.org/10.1017/jfm.2025.10514 Published online by Cambridge University Press

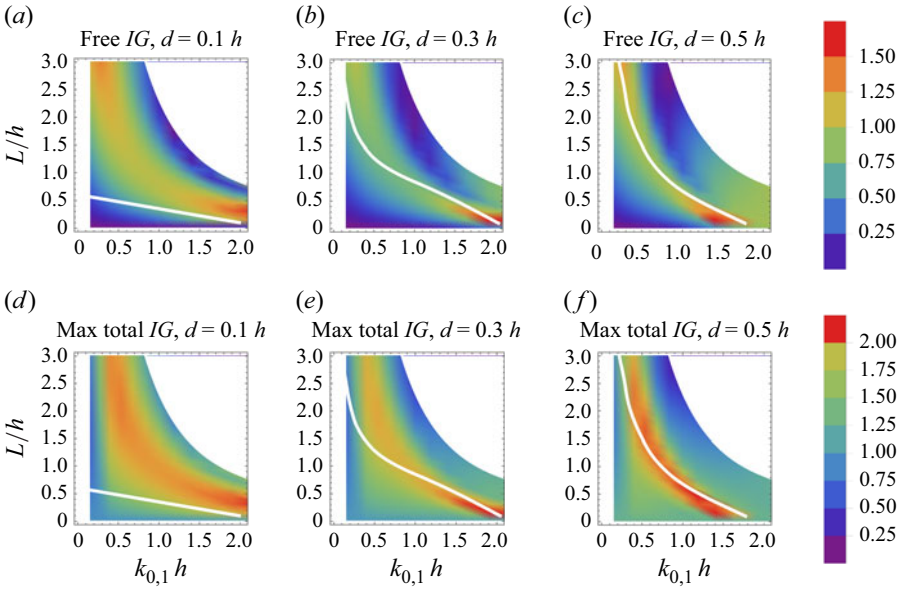


Figure 8. Panels (*a*), (*b*) and (*c*) show normalised amplitude of total free *IG* waves in the lee (region III) of a 2-D block. Panels (*d*), (*e*), (*f*) are similar, but for total *IG* waves. The white solid lines are locations of the 2-D block's RAO peaks (cf. row 2 of figure 7). In the white-coloured regions, the condition (7.1) is not met, and the results are not presented. This plot is similar to rows 4 and 5 of figure 7, except that the parameter L/h is varying continuously.

not apply to small-d cases (panels *a* and *d*), presumably because, according to row two of figure 7, the RAOs for the small-d cases are devoid of obvious peaks; hence, the RAO peak curve ceases to be a meaningful indicator.

Overall, when d is very large, a relationship exists between a block's linear RAO peak and its ability to attenuate transmitted total *IG* waves.

8.4. *A summary of heaving cases*

Compared with diffraction-only blocks, allowing heaving fundamentally changes the behaviour of *IG* waves around the block. From an *IG* wave reduction point of view, it is possible to reduce *IG* waves everywhere in the lee (region III) by up to 50 %, particularly for blocks with larger L and d, e.g. the $L = 1.5h$ and $2.0h$ cases with $d = 0.5h$, see the red dashed curves in figure 7(x, y), or figure 8(c, f).

9. Discussion and conclusions

9.1. *Some comments on viscous effects in the 2-D blocks' equations of motion*

All previous discussions assume that there is no damping when the 2-D blocks are heaving. A more realistic model should consider viscous damping due to e.g. power-take-off installed on WECs, and vortex generation during heaving motion. The viscous damping reduces the RAO peaks shown in figure 7 and generally shifts the peaks slightly towards the lower values of $k_{0,1}h$. The latter effect was investigated systematically by Cui *et al.* (2022). For *IG* waves, one may envisage that if the RAO peak can be shifted to a lower value of $k_{0,1}h$, the same block can control different *IG* waves, because figure 8 shows that *IG* wave is linked to the location of the RAO peaks. Unfortunately, this idea is not viable for the blocks considered in this paper, because the shift of the RAO peaks

https://doi.org/10.1017/jfm.2025.10514 Published online by Cambridge University Press

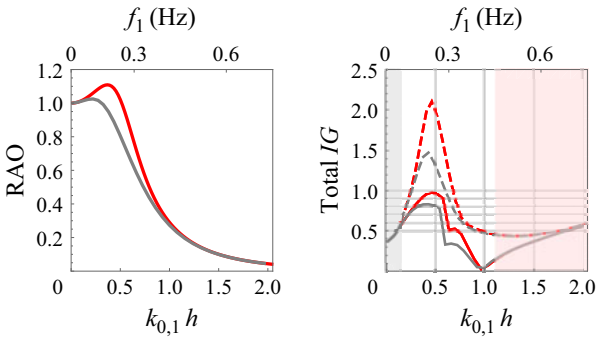


Figure 9. Effects of damping. Red curves in two panels are the same as the red curves in figure 7(*j*) and (*y*) ($L = 2h$, $d = 0.5h$). Grey curves: calculated with an empirical viscous term (see § C.4 in Appendix C) with the viscous parameter $\mathcal{K}_v$ set to 3×10^6. This figure is related to § 9.1.

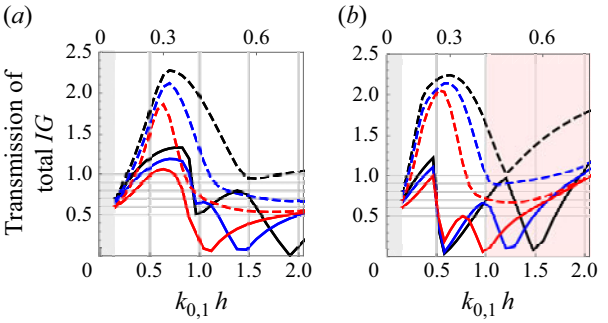


Figure 10. Effects of different modulation ratios. Similar to figure 7(*x*) ($L = 1.5h$), but instead of assuming $f_2 = 1.10\,f_1$, now the two cases feature $f_2 = 1.03\,f_1$ (*a*) and $f_2 = 1.15\,f_1$ (*b*). This figure is related to § 9.2.

towards low frequencies is not significant, and because an important ingredient of the total *IG* waves, *viz.* The radiated free *IG* wave (6.12), is not substantially affected by added damping, as their low frequency is usually far from heaving resonance.

An example is shown in figure 9: even when strong damping is applied, the total *IG* wave amplitude curves did not shift much in frequency, although it is interesting to note that the *IG* wave magnitudes are decreased for most values of $k_{0,1}h$.

9.2. *Other ratios of carrier frequencies*

Previous examples in this paper use $f_2 = 1.1\,f_1$. Two more ratios are discussed here: $f_2 = 1.03\,f_1$ and $f_2 = 1.15\,f_1$. It can be shown (details omitted here) using the analysis in Appendix A that, by choosing appropriate carrier wave amplitude ranges, the scaling in this paper still applies.

For brevity, only selected results are presented, see figure 10. The two panels of the figure are similar to figure 7(*x*), but using $f_2 = 1.03\,f_1$ and $f_2 = 1.15\,f_1$. For the former case, the condition (7.1) is satisfied for all values of $k_{0,1}h$. For the latter case, the condition (7.1) is satisfied up to $k_{0,1}h = 1.012$. From an *IG* wave reduction point of view, for the $f_2 = 1.03\,f_1$ case, the total *IG* wave is reduced for a wide range of $k_{0,1}h$ for both $d = 0.5h$ (red curves) and $d = 0.3h$ (blue curves) cases. For the $f_2 = 1.15\,f_1$ case, in the validity range $k_{0,1}h < 1.012$, the total *IG* wave is reduced for some values of $k_{0,1}h$. Overall, the figure demonstrates no qualitative difference from the $f_2 = 1.10\,f_1$ case.

https://doi.org/10.1017/jfm.2025.10514 Published online by Cambridge University Press

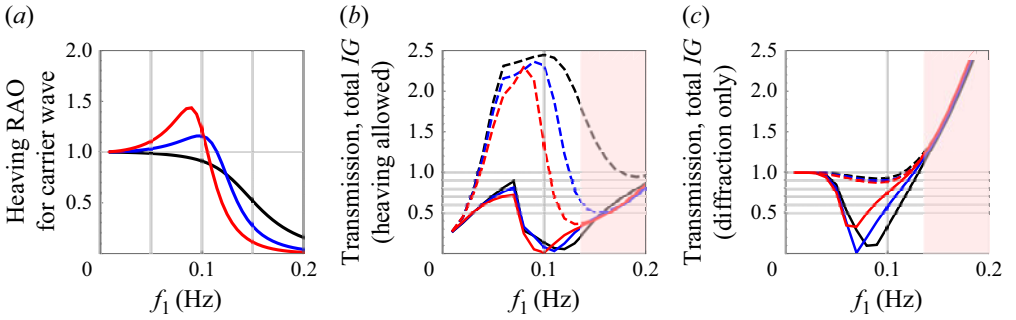


Figure 11. A dimensional example. (*a*) heaving RAO for 2-D heaving blocks with $L = 0.70h$. The water depth is $h = 30$ m. Black: $d = 0.10h$; blue: $d = 0.30h$; red: $d = 0.50h$. (*b*) normalised total *IG* wave in region III for heaving blocks; (*c*) similar to (*b*) but for diffraction-only blocks. In all cases, the two carrier wave frequencies satisfy $f_2 = 1.1 f_1$. In the red shaded regions, the condition (7.1) is not met, and the results may not be valid. Carrier wave amplitudes are $A_1 = A_2 = 2$ m. Note that the horizontal axis shows dimensional frequency f_1, not the non-dimensional parameter $k_{0,1}h$.

9.3. *A physical example using dimensional parameters*

All calculations so far are performed with parameters consistent with laboratory conditions ($h = 1$ m, $f_1 > 0.15$ Hz), and used the non-dimensional wavenumber $k_{0,1}h$ extensively. Here, we revert to the dimensional parameter f_1 (the frequency of the first linear carrier wave), and consider an example physically relevant to coastal waters and floating structures. Assume the water depth is $h = 30$ m, relevant to some coastal zones (e.g. McComb *et al.* 2009), and assume the 2-D block's half-breadth is $L = 0.7h = 21$ m, i.e. the full breadth is $2L = 42$ m, relevant to some floating structures such as some types of ships. The draughts are chosen to be $d = 0.1h$, $0.3h$ and $0.5h$. The condition (7.1) is satisfied for $f_1 < 0.137$ Hz; however, figure 11(*b*, *c*) presents *IG* wave transmission results up to 0.2 Hz, with red shading marking regions that violate condition (7.1).

The main finding in figure 11(*b*) is that, when heaving is allowed, the total *IG* wave transmission can be reduced for some values of f_1, particularly when $d = 0.5h$, while the diffraction-only cases in figure 11(*c*) cannot achieve this.

9.4. *Conclusions*

This paper studies 2-D heaving and stationary blocks. These blocks' draught d is less than half of the local water depth h, and their lengths $2L$ are, in general, smaller than $1/20$ of the length of the *IG* wave, which is two times the length of the wave group. In some cases, the length restriction is violated; the results of these cases are still shown, with cautionary notes (see e.g. the light red regions in figures 5 and 7). The main contributions of this paper are:

(i) generalise the method of Liu & Iskandarani (1991) and Hossain *et al.* (2001) by allowing device motion, using heave as an example;
(ii) discover that heaving resolves the problem regarding free *IG* wave management found in e.g. Liu & Iskandarani (1991);
(iii) discover that relatively small heaving devices can modify *IG* waves from an offshore location before the 'troublesome' free *IG* waves are released by near-shore bathymetry changes. This differs from Gao *et al.* (2021), where relatively large-scale infrastructure is needed to control *IG* waves;
(iv) provide new results applicable to emerging applications such as multiple-purpose wave energy arrays (Sergiienko *et al.* 2024).

https://doi.org/10.1017/jfm.2025.10514 Published online by Cambridge University Press

This study has limitations: (i) the ratio between the wavenumber of the two incident carrier waves is fixed to a few numbers; (ii) the 2-D blocks are infinitely long in the spanwise direction; but real blocks are finite, and 3-D effects should be considered. For isolated 3-D objects such as a single cylindrical heaving buoy, the radiated waves decay quickly and can be omitted in the analysis of *IG* waves (Wu & Liu 1990). For such cases, the conclusions of this paper are unlikely to apply; (iii) the flow is assumed to be inviscid, which leads to an overestimation of a 2-D block's heaving amplitude. A formal discussion of viscous effects is not given, although an empirical discussion is provided in § 9.1; (iv) the method cannot deal with blocks whose lengths are not small compared with the length of *IG* waves; (v) the paper assumes a flat bathymetry; (vi) in the real ocean, the wave field is unlikely to contain only two carrier waves as it is assumed here, but contains other frequency components; (vii) a quantitative comparison of the current results with Sergiienko *et al.* (2024) is not attempted, because the 2-D heaving blocks used here differ in detail from the quasi-infinite OWC arrays despite both generating long-crested y-independent waves.

Some specific findings are now revisited. The classic linear diffraction and radiation problems are solved by eigenfunction expansion. The resulting diffracted and radiated carrier waves are then used to calculate bound *IG* waves via an equation derivable from multiple-scale analysis. A semi-analytical method then evaluates free *IG* waves, which, when combined with the aforementioned bound *IG* waves, ensures that the *IG* wave potential is continuous across the block. Such a free *IG* wave excites the block to heaving motion, which further spawns radiated free *IG* waves.

When all bound and free *IG* waves are combined, the resulting total *IG* waves generally differ from the incident *IG* waves. Four factors dictate the extent of *IG* wave modifications in the lee (region III in figure 2) of the block: first, the reduction of bound *IG* waves due to reduction of carrier waves via diffraction; second, the modification of bound *IG* waves due to radiated carrier waves; third, the generation of induced free *IG* waves to match the total *IG* wave potential and flux across the block; fourth, the generation of radiated free *IG* waves due to second-order heaving motion of the block. The second and fourth factors are absent in the case of diffraction-only blocks.

The results can be classified into three scenarios: (i) a significant decrease in the total *IG* wave amplitude everywhere in the lee of the block; (ii) a significant decrease in total *IG* wave amplitude at some locations with noticeable increases at the other locations; (iii) a significant decrease in total *IG* wave amplitude at some locations, but an unchanged *IG* wave (or a small modification) at the other locations. When reducing the total *IG* waves is the objective, scenario (i) should be pursued; when amplifying *IG* waves is needed, scenario (ii) is better.

The diffraction-only cases in figure 5 generally yield scenario (iii), suggesting that they are not optimal for *IG* wave reduction and amplification. From an oceanographic point of view, many natural objects are stationary (diffraction only), such as underwater sandbars, rocks and reefs. These are usually bottom mounted, as opposed to the floating blocks discussed in this paper; hence, the quantitative details may not apply to them. A discussion of these objects is straightforward using the method of this study.

As for the heaving blocks in figure 7, for the shallow-draft ($d = 0.1h, 0.3h$) cases, scenarios (ii) and (iii) are more prevalent. Cases of scenario (i) occur primarily for the deep-draft (e.g. $d = 0.5$) blocks at some wavenumber, e.g. the red curves in figures 7(x) and 7(y). The reduction of *IG* waves everywhere in the lee of a block can reach approximately 50 % in figure 7(y). This is achieved with only one small heaving block. From an oceanographic point of view, this hints that the heaving motion of floating objects (such as some icebergs) can modify *IG* waves and impact the environment behind them.

https://doi.org/10.1017/jfm.2025.10514 Published online by Cambridge University Press

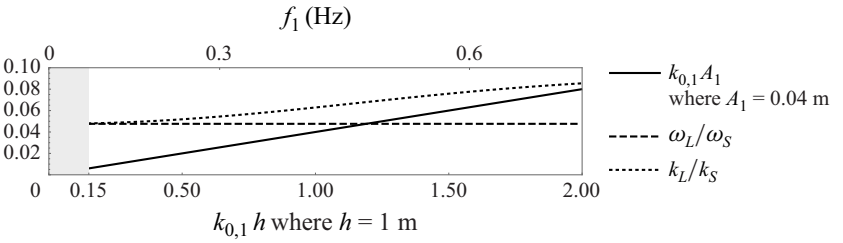


Figure 12. Comparing the wave steepness $k_{0,1}A_1 \equiv \varepsilon$ against two ratios, ω_L/ω_S and k_L/k_S, showing that these quantities are of the same order of magnitude for most values of $k_{0,1}h$ discussed in this work. This is relevant to Appendix A.

In conclusion, we show that small heaving 2-D blocks can attenuate transmitted *IG* waves; this is a step towards explaining the *IG* wave attenuation observed by Sergiienko *et al.* (2024).

Acknowledgements. The authors thank anonymous reviewers for providing constructive feedback.

Funding. This work received funding from the Australian Research Council (grant number: LP180101109). A.-R.W. is funded by a PhD scholarship from the University of Adelaide. L.G.B. is funded by an Australian Research Council Future Fellowship (FT190100404). N.Y.S. received an Australian Research Council Early Career Industry Fellowship (IE230100545).

Declaration of interests. The authors report no conflict of interest.

Appendix A. Justification of scaling in perturbation expansions

The small parameter ε defined as wave steepness, $\varepsilon \equiv k_{0,1}A_1$, is used both to expand Φ, η and to characterise the slow temporal and spatial scales in the multiple-scale expansion (cf. § 2.1). Figure 12 justifies this through a calculation example. First, $\varepsilon = k_{0,1}A_1$ is plotted against $k_{0,1}h$ assuming $h = 1$ m and $A_1 = 0.04$ m (these are assumptions underlying most of the examples in this work). Second, the ratio between the 'slow' frequency ω_L (see 4.2) and the 'fast' frequency ω_S (also given by 4.2) is plotted. Third, the ratio between the 'slow' and 'fast' wavenumbers k_L/k_S (4.2) is plotted. For most values of $k_{0,1}h$, these ratios are of the same order of magnitude as ε, hence ε can be employed to characterise the slow scales. For very small $k_{0,1}h$, ε can be much smaller than these ratios; however, in these cases, by increasing wave amplitude A_1, this can be rectified (not shown in the figure). Hence, one can generally choose A_1 such that ε can be used to characterise slow scales in the multiple-scale expansion. As long as A_1 is not too large, it generally does not affect the main objective of this work (*IG* wave modification).

Appendix B. The linear diffraction problem for the 2-D floating block

The coefficients for diffracted waves in (3.6) are determined. The governing equations are (2.9) and (3.1). The eigenfunction expansion method (e.g. Linton & McIver 2001) is applied to study a monochromatic case with an arbitrary frequency, and the method extends to other frequencies. The approach follows Yiew (2017) and Westcott *et al.* (2024), but more details are provided. The results are validated against Lee (1995) who used a similar method.

Use Φ^D to denote the diffraction potential. Periodicity in time suggests

$$\Phi^D(\mathfrak{x}, z, \mathfrak{t}) = \mathrm{Re}\left\{\frac{\mathrm{g}}{\mathrm{i}\omega}\phi^D(x, z)\mathrm{e}^{-\mathrm{i}\omega\mathrm{t}}\right\}, \tag{B1}$$

https://doi.org/10.1017/jfm.2025.10514 Published online by Cambridge University Press

where ϕ^D is unknown. Substituting (B1) into (2.9) and (3.1) and simplifying, we obtain equations for ϕ^D

$$\frac{\partial^2\phi^D}{\partial\mathfrak{x}^2}+\frac{\partial^2\phi^D}{\partial z^2}=0;\quad \frac{\partial\phi^D}{\partial z}=\frac{\omega^2}{\mathrm{g}}\phi^D\bigg|_{z=0};\quad \eta=\mathrm{Re}\left\{\phi^D\mathrm{e}^{-\mathrm{i}\omega\mathfrak{t}}\right\}\bigg|_{z=0}.$$
$$\frac{\partial\phi^D}{\partial z}=0\bigg|_{z=-h};\quad \frac{\partial\phi^D}{\partial n}=0\bigg|_{\text{on } s_{1,2,3}}. \tag{B2}$$

B.1. *Solutions: with N evanescent modes*

Equation (B2) is examined in three regions in figure 2. Denote ϕ^D in regions I, II, III by $\phi^{\mathrm{I},D}$, $\phi^{\mathrm{II},D}$ and $\phi^{\mathrm{III},D}$. We have

$$\phi^{\mathrm{I},D}=\sum_{n=0}^{N}\left[a_n^+\mathrm{e}^{\mathrm{i}k_n(\mathfrak{x}-(-L))}+a_n^-\mathrm{e}^{-\mathrm{i}k_n(\mathfrak{x}-(-L))}\right]\psi_n(z),\ \text{where } \psi_n=\frac{\cosh k_n(z+h)}{\cosh k_nh}, \tag{B3}$$

in which k_0 is the solution to $\omega^2=\mathrm{g}k_0\tanh k_0h$. For $n>0$, $k_n=-\mathrm{i}K_n$, where K_n is the solution to $\omega^2=-\mathrm{g}K_n\tan K_nh$. Similarly, in region III, $\phi^{\mathrm{III},D}$ is expanded as

$$\phi^{\mathrm{III},D}=\sum_{n=0}^{N}\left[b_n^+\mathrm{e}^{\mathrm{i}k_n(\mathfrak{x}-L)}+b_n^-\mathrm{e}^{-\mathrm{i}k_n(\mathfrak{x}-L)}\right]\psi_n(z). \tag{B4}$$

The coefficients a_n^+ in (B3) describe incident waves travelling to the right, b_n^- in (B4) describe incident waves travelling to the left, whilst a_n^- and b_n^+ are coefficients for reflected and transmitted waves. It is assumed that incident waves are right-travelling only, with no evanescent modes, so $b_n^-=0$ for all n, and $a_n^+=0$ for $n>0$, while $a_0^+=A\mathrm{e}^{-\mathrm{i}k_0L}$ where A is the amplitude of the incident wave, so

$$a_0^+\mathrm{e}^{\mathrm{i}k_0(\mathfrak{x}-(-L))}=A\mathrm{e}^{-\mathrm{i}k_0L}\mathrm{e}^{\mathrm{i}k_0(\mathfrak{x}-(-L))}=A\mathrm{e}^{-\mathrm{i}k_0L}\mathrm{e}^{\mathrm{i}k_0(\mathfrak{x}+L)}=A\mathrm{e}^{\mathrm{i}k_0\mathfrak{x}}. \tag{B5}$$

The potential $\phi^{\mathrm{II},D}$ for region II assumes the following form:

$$\phi^{\mathrm{II},D}=\left(\alpha_0^+\mathfrak{x}+\alpha_0^-\right)\zeta_0+\sum_{n=1}^{N}\left[\alpha_n^+\mathrm{e}^{\mathrm{i}\kappa_n(\mathfrak{x}-(-L))}+\alpha_n^-\mathrm{e}^{-\mathrm{i}\kappa_n(\mathfrak{x}-L)}\right]\zeta_n(z), \tag{B6}$$

where α_0^+ and α_0^- are unknown coefficients, and

$$\zeta_n=\frac{\cosh\kappa_n(z+h)}{\cosh\kappa_n(h-d)},\quad \kappa_n=n\frac{\mathrm{i}\pi}{h-d}. \tag{B7}$$

B.2. *Matching conditions*

Matching the velocity potential from region I to region II at $\mathfrak{x}=-L$ and from region II to region III at $\mathfrak{x}=L$ requires

$$\phi^{\mathrm{I},D}=\phi^{\mathrm{II},D}\bigg|_{\mathfrak{x}=-L},\ \text{and}\ \ \phi^{\mathrm{III},D}=\phi^{\mathrm{II},D}\bigg|_{\mathfrak{x}=L},\ \text{for } z\in[-h,-d]. \tag{B8}$$

https://doi.org/10.1017/jfm.2025.10514 Published online by Cambridge University Press

Matching flux from region I to region II at $\mathfrak{x} = -L$ and flux from region II to region III at $\mathfrak{x} = L$ requires

$$\frac{\partial \phi^{\mathrm{I},D}}{\partial \mathfrak{x}} = \begin{cases} \left.\dfrac{\partial \phi^{\mathrm{II},D}}{\partial \mathfrak{x}}\right|_{\mathfrak{x}=-L}, & z \in [-h, -d] \\ 0, & z \in [-d, 0] \end{cases}, \text{ and } \frac{\partial \phi^{\mathrm{III},D}}{\partial \mathfrak{x}} = \begin{cases} \left.\dfrac{\partial \phi^{\mathrm{II},D}}{\partial \mathfrak{x}}\right|_{\mathfrak{x}=L}, & z \in [-h, -d] \\ 0, & z \in [-d, 0] \end{cases}. \tag{B9}$$

The above matching conditions are turned to systems of algebraic equations with which the unknown coefficients are solved, using the following inner products:

$$\int_{-h}^{-d} (\cdot)\zeta_m \mathrm{d}z, \text{ and } \int_{-h}^{0} (\cdot)\psi_m \mathrm{d}z, \ m = 0, 1, 2, \ldots, N. \tag{B10}$$

B.3. *Surface elevations of linear diffracted waves*

Once $\phi^{\mathrm{I},D}$, $\phi^{\mathrm{II},D}$ and $\phi^{\mathrm{III},D}$ are determined, (B2) suggests that the surface elevation of diffracted waves is determined by $\eta = \mathrm{Re}\{\phi^D \mathrm{e}^{-\mathrm{i}\omega \mathfrak{t}}\}|_{z=0}$. The incident potential function $\phi^{\mathrm{I},A}$ constitutes the a_n^+ terms of $\phi^{\mathrm{I},D}$ plus the b_n^- terms of $\phi^{\mathrm{III},D}$, being

$$\phi^{\mathrm{I},A} = \begin{cases} \sum_{n=0}^{N} a_n^+ \mathrm{e}^{\mathrm{i}k_n(\mathfrak{x}-(-L))}\psi_n(z), & \mathfrak{x} < -L, \\ \sum_{n=0}^{N} b_n^- \mathrm{e}^{-\mathrm{i}k_n(\mathfrak{x}-L)}\psi_n(z), & \mathfrak{x} > L. \end{cases} \tag{B11}$$

Because in this paper it is assumed that $b_n^- = 0, a_n^+ = 0$ (for $n > 0$), and that $a_0^+ = A\mathrm{e}^{-\mathrm{i}k_0 L}$, it follows that $\phi^{\mathrm{I},A} = A\mathrm{e}^{\mathrm{i}k_0 \mathfrak{x}}\psi_0(z), \ \mathfrak{x} < -L$, where $\psi_0(0) = 1$. The surface elevation of the incident wave is hence $\eta^{\mathrm{I},A} = \mathrm{Re}\{\phi^{\mathrm{I},A}\mathrm{e}^{-\mathrm{i}\omega \mathfrak{t}}\}|_{z=0} = A\cos(k_0 x - \omega \mathfrak{t})$, leading to (3.4). The reflected waves' potential function $\phi^{\mathrm{I},D}$ involves the a_n^- terms of $\phi^{\mathrm{I},D}$, being

$$\phi^{\mathrm{I},D} = \sum_{n=0}^{N} a_n^- \mathrm{e}^{-\mathrm{i}k_n(\mathfrak{x}-(-L))}\psi_n(z), \ \mathfrak{x} < -L. \tag{B12}$$

The surface elevation of reflected waves then reads

$$\begin{aligned} \eta^{\mathrm{I},D} &= \mathrm{Re}\left\{\phi^{\mathrm{I},D}\mathrm{e}^{-\mathrm{i}\omega \mathfrak{t}}\right\}\big|_{z=0}, \ \mathfrak{x} < -L \\ &= |a_0^-| \cos\left[-k_0(\mathfrak{x} - (-L)) - \omega \mathfrak{t} + \arg(a_0^-)\right] \\ &\quad + \mathrm{Re}\left\{\sum_{n=1}^{N} a_n^- \mathrm{e}^{\mathrm{i}[-k_n(\mathfrak{x}-(-L))-\omega \mathfrak{t}]}\right\}, \ \mathfrak{x} < -L. \end{aligned} \tag{B13}$$

The transmitted waves' potential function $\phi^{\mathrm{III},D}$ involves the b_n^+ terms of $\phi^{\mathrm{III},D}$ and leads to the following surface elevation:

$$\eta^{\mathrm{III},D} = |b_0^+| \cos\left[k_0(\mathfrak{x} - L) - \omega \mathfrak{t} + \arg(b_0^+)\right] + \mathrm{Re}\left\{\sum_{n=1}^{N} b_n^+ \mathrm{e}^{\mathrm{i}[k_n(\mathfrak{x}-L)-\omega \mathfrak{t}]}\right\}, \ \mathfrak{x} > L. \tag{B14}$$

Discard evanescent modes to obtain (3.6*a*) and (3.6*c*).

https://doi.org/10.1017/jfm.2025.10514 Published online by Cambridge University Press

Appendix C. The linear radiation problem for the 2-D floating block

The coefficients for radiated waves in (3.6) are determined. The procedures still follow Yiew (2017) and Westcott *et al.* (2024). Introduce a heaving radiation potential Φ^R

$$\Phi^R(\mathfrak{x}, z, \mathfrak{t}) = \mathrm{Re}\left\{\frac{\mathrm{g}}{\mathrm{i}\omega}\phi^R(\mathfrak{x}, z)\mathrm{e}^{-\mathrm{i}\omega\mathfrak{t}}\right\}, \tag{C1}$$

where ϕ^R is unknown. Substituting the above to (2.9), (3.1), and (3.3), the governing equations for ϕ^R are the same in form as (B2) with an additional boundary condition

$$\frac{\mathrm{g}}{\mathrm{i}\omega}\frac{\partial\phi^R}{\partial z}\mathrm{e}^{-\mathrm{i}\omega\mathfrak{t}} = -\mathrm{i}\omega A_h\mathrm{e}^{-\mathrm{i}\omega\mathfrak{t}}\Big|_{\text{on } s_2} \Rightarrow \frac{\partial\phi^R}{\partial z} = \frac{\omega^2}{\mathrm{g}}A_h\Big|_{z=-d,\,-L<\mathfrak{x}<L}. \tag{C2}$$

where A_h is the unknown heaving amplitude introduced in (3.2).

C.1. *Flow potentials and matching conditions*

Denote ϕ^R in regions I, II, III by $\phi^{\mathrm{I},R}$, $\phi^{\mathrm{II},R}$, $\phi^{\mathrm{III},R}$, then the waves corresponding to $\phi^{\mathrm{I},R}$ should travel away from the block (left going), while the waves related to $\phi^{\mathrm{III},R}$ should be right going. Accordingly, the following eigenfunction expansions are used:

$$\phi^{\mathrm{I},R} = \sum_{n=0}^{N}\mathfrak{a}_n^-\mathrm{e}^{-\mathrm{i}k_n(\mathfrak{x}-(-L))}\psi_n(z) \text{ and } \phi^{\mathrm{III},R} = \sum_{n=0}^{N}\mathfrak{b}_n^+\mathrm{e}^{\mathrm{i}k_n(\mathfrak{x}-L)}\psi_n(z), \tag{C3}$$

where the Gothic letters $\mathfrak{a}_n^-$ and $\mathfrak{b}_n^+$ should be distinguished from the diffraction coefficients a_n and b_n. The eigenfunctions in region II need to satisfy the additional boundary condition equation (C2), resulting in

$$\begin{aligned}\phi^{\mathrm{II},R} = {}& \left(\beta_0^+\mathfrak{x} + \beta_0^-\right)\zeta_0 + \sum_{n=1}^{N}\left[\beta_n^+\mathrm{e}^{\mathrm{i}\kappa_n(\mathfrak{x}-(-L))} + \beta_n^-\mathrm{e}^{-\mathrm{i}\kappa_n(\mathfrak{x}-L)}\right]\zeta_n(z)\\ &+ \frac{\omega^2}{\mathrm{g}}A_h\frac{(z+h)^2-\mathfrak{x}^2}{2(h-d)}.\end{aligned} \tag{C4}$$

The matching conditions across the three regions are similar to those in Appendix B.2. The added unknown A_h requires an added equation, specified in the ensuing subsection.

C.2. *Added mass, radiation damping and a force balance equation for heaving amplitude*

The heaving amplitude A_h in (3.2) is decided by a force balance equation. Neglecting viscous effects, the ingredient of this equation involves the incident wave's excitation force, the restoring force, the inertia force and a radiation force (related to added mass and radiation damping).

The radiation force (e.g. Mei *et al.* 2005; Falnes & Kurniawan 2020) reads

$$F^R = \int_{-L}^{L} -\rho\frac{\partial\Phi^{\mathrm{II},R}}{\partial t}\Big|_{z=-d}\mathrm{d}\mathfrak{x} = \rho\mathrm{g}\mathrm{e}^{-\mathrm{i}\omega\mathfrak{t}}\int_{-L}^{L}\phi^{\mathrm{II},R}(\mathfrak{x}, z)\Big|_{z=-d}\mathrm{d}\mathfrak{x}, \tag{C5}$$

where $\phi^{\mathrm{II},R}$ is given by (C4). The integration in (C5) can be cast into the following form, separating real and imaginary parts:

$$\int_{-L}^{L}\phi^{\mathrm{II},R}\Big|_{z=-d}\mathrm{d}\mathfrak{x} = \mathrm{Re}\left\{\int_{-L}^{L}\phi^{\mathrm{II},R}\Big|_{z=-d}\mathrm{d}\mathfrak{x}\right\} + \mathrm{iIm}\left\{\int_{-L}^{L}\phi^{\mathrm{II},R}\Big|_{z=-d}\mathrm{d}\mathfrak{x}\right\}, \tag{C6}$$

https://doi.org/10.1017/jfm.2025.10514 Published online by Cambridge University Press

with which (C5) becomes

$$\begin{aligned} F^R &= \rho g e^{-i\omega t} \mathrm{Re}\left\{\int_{-L}^{L} \phi^{\mathrm{II},R}\Big|_{z=-d} \mathrm{d}\mathfrak{x}\right\} + i\rho g e^{-i\omega t} \mathrm{Im}\left\{\int_{-L}^{L} \phi^{\mathrm{II},R}\Big|_{z=-d} \mathrm{d}\mathfrak{x}\right\} \\ &= \rho g e^{-i\omega t} \frac{\ddot{\xi}}{-i\omega} \frac{\mathrm{Re}\left\{\int_{-L}^{L} \phi^{\mathrm{II},R}\big|_{z=-d} \mathrm{d}\mathfrak{x}\right\}}{\dot{\xi}} + i\rho g e^{-i\omega t} \dot{\xi} \frac{\mathrm{Im}\left\{\int_{-L}^{L} \phi^{\mathrm{II},R}\big|_{z=-d} \mathrm{d}\mathfrak{x}\right\}}{\dot{\xi}} \\ &= -\rho \ddot{\xi} \frac{\mathrm{Re}\left\{\int_{-L}^{L} \phi^{\mathrm{II},R}\big|_{z=-d} \mathrm{d}\mathfrak{x}\right\}}{\frac{\omega^2}{g} A_h} - \rho\omega\dot{\xi} \frac{\mathrm{Im}\left\{\int_{-L}^{L} \phi^{\mathrm{II},R}\big|_{z=-d} \mathrm{d}\mathfrak{x}\right\}}{\frac{\omega^2}{g} A_h} \\ &= -\ddot{\xi} m_a - \dot{\xi} R, \end{aligned} \tag{C7}$$

where m_a and R are added mass and radiation damping.

The excitation force that drives heaving motion is due to the diffraction potential $\phi^{\mathrm{II},D}$ (cf. B6) in region II

$$F^D = \int_{-L}^{L} -\rho \frac{\partial \phi^{\mathrm{II},D}}{\partial t}\Big|_{z=-d} \mathrm{d}\mathfrak{x} = \rho g e^{-i\omega t} \int_{-L}^{L} \phi^{\mathrm{II},D}(\mathfrak{x}, z)\Big|_{z=-d} \mathrm{d}\mathfrak{x}. \tag{C8}$$

The restoring force (hydrodynamic stiffness) for a block with unit width is $F^S = \rho g A_{wp} \xi$, where A_{wp} is the waterplane area that equals $2L$.

The inertia force is proportional to the acceleration of the block: $F^M = m\ddot{\xi}$, where $m = 2L\rho d$ is the mass of the block with unit width.

Balancing all forces by $F^M + F^S = F^D + F^R$ and using $\dot{\xi}(\mathrm{t}) = -i\omega A_h e^{-i\omega t}$, etc. leads to an equation for A_h

$$-\omega^2(2L\rho d + m_a)A_h - i\omega R A_h + 2L\rho g A_h = \rho g \int_{-L}^{L} \phi^{\mathrm{II},D}(\mathfrak{x}, z)\Big|_{z=-d} \mathrm{d}\mathfrak{x}, \tag{C9}$$

from which A_h is found as

$$A_h = \frac{\rho g \int_{-L}^{L} \phi^{\mathrm{II},D}(\mathfrak{x}, z)\big|_{z=-d} \mathrm{d}\mathfrak{x}}{-\omega^2(2L\rho d + m_a) - i\omega R + 2L\rho g}. \tag{C10}$$

C.3. *Surface elevation of radiated waves*

The reflected (left-travelling) and transmitted (right-travelling) wave potentials denoted by $\phi^{\mathrm{I},R}$ and $\phi^{\mathrm{III},R}$ are given by (C3). Then, the surface elevations of radiated waves equation can be calculated be (2.9)

$$\eta^R = \mathrm{Re}\left\{\phi^R e^{-i\omega t}\right\}\big|_{z=0}. \tag{C11}$$

Hence the surface elevations of reflected and transmitted radiated waves are

$$\begin{aligned} \eta^{\mathrm{I},R} &= \mathrm{Re}\left\{\phi^{\mathrm{I},R} e^{-i\omega t}\right\}\big|_{z=0}, \ \mathfrak{x} < -L \\ &= \left|\mathfrak{a}_0^-\right| \cos\left[-k_0(\mathfrak{x} - (-L)) - \omega t + \arg\left(a_0^-\right)\right] \\ &\quad + \mathrm{Re}\left\{\sum_{n=1}^{N} \mathfrak{a}_n^- e^{i[-k_n(\mathfrak{x}-(-L))-\omega t]}\right\}, \ \mathfrak{x} < -L, \end{aligned} \tag{C12}$$

https://doi.org/10.1017/jfm.2025.10514 Published online by Cambridge University Press

$$\eta^{\mathrm{III},R} = |\mathfrak{b}_0^+| \cos\left[k_0(\mathfrak{x}-L) - \omega\mathfrak{t} + \arg(\mathfrak{b}_0^+)\right] + \mathrm{Re}\left\{\sum_{n=1}^{N} \mathfrak{b}_n^+ \mathrm{e}^{\mathrm{i}[k_n(\mathfrak{x}-L)-\omega\mathfrak{t}]}\right\}, \quad \mathfrak{x} > L. \tag{C13}$$

Discarding evanescent modes, one obtains the radiated waves in (3.6*b*, *d*).

C.4. *A note on viscous damping*

To include viscous damping, an empirical viscous damping term with a real viscous damping coefficient $\mathcal{K}_v$ (e.g. Cui *et al.* 2023) is added to the force balance equation (C9), for it to become

$$-\omega^2(2L\rho d + m_a)A_h - \mathrm{i}\omega\left(R + \mathcal{K}_v\frac{8\omega}{3\pi}|A_h|\right)A_h + 2L\rho\mathrm{g}A_h = \rho\mathrm{g}\int_{-L}^{L}\phi^{\mathrm{II},D}(\mathfrak{x},z)\Big|_{z=-d}\mathrm{d}\mathfrak{x}. \tag{C14}$$

So A_h is now

$$A_h = \frac{\rho\mathrm{g}\int_{-L}^{L}\phi^{\mathrm{II},D}(\mathfrak{x},z)\big|_{z=-d}\,\mathrm{d}\mathfrak{x}}{-\omega^2(2L\rho d + m_a) - \mathrm{i}\omega\left(R + \mathcal{K}_v\dfrac{8\omega}{3\pi}|A_h|\right) + 2L\rho\mathrm{g}}, \tag{C15}$$

which is an equation for A_h, as it contains A_h on both sides. It is to be solved iteratively.

Appendix D. Details of bound *IG* wave potentials

Bound *IG* waves mentioned in § 4 are given in this appendix. Since the incident bound *IG* wave potential is already given by (4.3), it is not repeated below. Other bound *IG* wave potentials are as follows.

D.1. *Bound IG wave potentials in region I*

$$\Phi_{bIG}^{\mathrm{I},D_1D_2} = C_B\left|a_{0,1}^-\right\|a_{0,2}^-\left|\left[\mathrm{e}^{-2\mathrm{i}k_L(X+L)}\mathrm{e}^{-2\mathrm{i}\omega_L T}\mathrm{e}^{2\mathrm{i}\gamma_{IG}^{\mathrm{I},D_1D_2}} - \mathrm{c.c.}\right], \tag{D1a}$$

$$\Phi_{bIG}^{\mathrm{I},R_1R_2} = C_B\left|\mathfrak{a}_{0,1}^-\right\|\mathfrak{a}_{0,2}^-\left|\left[\mathrm{e}^{-2\mathrm{i}k_L(X+L)}\mathrm{e}^{-2\mathrm{i}\omega_L T}\mathrm{e}^{2\mathrm{i}\gamma_{IG}^{\mathrm{I}R_1R_2}} - \mathrm{c.c.}\right], \tag{D1b}$$

$$\Phi_{bIG}^{\mathrm{I},D_1R_2} = C_B\left|a_{0,1}^-\right\|\mathfrak{a}_{0,2}^-\left|\left[\mathrm{e}^{-2\mathrm{i}k_\mathrm{L}(X+L)}\mathrm{e}^{-2\mathrm{i}\omega_\mathrm{L}T}\mathrm{e}^{2\mathrm{i}\gamma_{IG}^{\mathrm{I},\mathrm{D}_1\mathrm{R}_2}} - \mathrm{c.c.}\right], \tag{D1c}$$

$$\Phi_{bIG}^{\mathrm{I},D_2R_1} = C_B\left|a_{0,2}^-\right\|\mathfrak{a}_{0,1}^-\left|\left[\mathrm{e}^{-2\mathrm{i}k_L(X+L)}\mathrm{e}^{-2\mathrm{i}\omega_L T}\mathrm{e}^{2\mathrm{i}\gamma_{IG}^{\mathrm{I},D_2R_1}} - \mathrm{c.c.}\right], \tag{D1d}$$

where the phase angles are

$$\gamma_{IG}^{\mathrm{I},D_1D_2} = \frac{\arg\left(a_{0,1}^-\right) - \arg\left(a_{0,2}^-\right)}{2}, \tag{D2a}$$

$$\gamma_{IG}^{\mathrm{I},R_1R_2} = \frac{\arg\left(\mathfrak{a}_{0,1}^-\right) - \arg\left(\mathfrak{a}_{0,2}^-\right)}{2}, \tag{D2b}$$

$$\gamma_{IG}^{\mathrm{I},D_1R_2} = \frac{\arg\left(a_{0,1}^-\right) - \arg\left(\mathfrak{a}_{0,2}^-\right)}{2}, \tag{D2c}$$

$$\gamma_{IG}^{\mathrm{I},D_2R_1} = \frac{\arg\left(a_{0,2}^-\right) - \arg\left(\mathfrak{a}_{0,1}^-\right)}{2}. \tag{D2d}$$

https://doi.org/10.1017/jfm.2025.10514 Published online by Cambridge University Press

D.2. *Bound IG wave potentials in region III*

$$\Phi_{bIG}^{\mathrm{III},D_1D_2} = C_B\big|b_{0,1}^{+}\big\|b_{0,2}^{+}\big|\big[\mathrm{e}^{2\mathrm{i}k_L(X-L)}\mathrm{e}^{-2\mathrm{i}\omega_L T}\mathrm{e}^{2\mathrm{i}\gamma_{IG}^{\mathrm{III},D_1D_2}} - \mathrm{c.c.}\big], \tag{D3a}$$

$$\Phi_{bIG}^{\mathrm{III},R_1R_2} = C_B\big|\mathfrak{b}_{0,1}^{+}\big\|\mathfrak{b}_{0,2}^{+}\big|\big[\mathrm{e}^{2\mathrm{i}k_L(X-L)}\mathrm{e}^{-2\mathrm{i}\omega_L T}\mathrm{e}^{2\mathrm{i}\gamma_{IG}^{\mathrm{III},R_1R_2}} - \mathrm{c.c.}\big], \tag{D3b}$$

$$\Phi_{bIG}^{\mathrm{III},D_1R_2} = C_B\big|b_{0,1}^{+}\big\|\mathfrak{b}_{0,2}^{+}\big|\big[\mathrm{e}^{2\mathrm{i}k_L(X-L)}\mathrm{e}^{-2\mathrm{i}\omega_L T}\mathrm{e}^{2\mathrm{i}\gamma_{IG}^{\mathrm{III},D_1R_2}} - \mathrm{c.c.}\big], \tag{D3c}$$

$$\Phi_{bIG}^{\mathrm{III},D_2R_1} = C_B\big|b_{0,2}^{+}\big\|\mathfrak{b}_{0,1}^{+}\big|\big[\mathrm{e}^{2\mathrm{i}k_L(X-L)}\mathrm{e}^{-2\mathrm{i}\omega_L T}\mathrm{e}^{2\mathrm{i}\gamma_{IG}^{\mathrm{III},D_2R_1}} - \mathrm{c.c.}\big], \tag{D3d}$$

where

$$\gamma_{IG}^{\mathrm{III},D_1D_2} = \frac{\arg\big(b_{0,1}^{+}\big) - \arg\big(b_{0,2}^{+}\big)}{2}, \tag{D4a}$$

$$\gamma_{IG}^{\mathrm{III},R_1R_2} = \frac{\arg\big(\mathfrak{b}_{0,1}^{+}\big) - \arg\big(\mathfrak{b}_{0,2}^{+}\big)}{2}, \tag{D4b}$$

$$\gamma_{IG}^{\mathrm{III},D_1R_2} = \frac{\arg\big(b_{0,1}^{+}\big) - \arg\big(\mathfrak{b}_{0,2}^{+}\big)}{2}, \tag{D4c}$$

$$\gamma_{IG}^{\mathrm{III},D_2R_1} = \frac{\arg\big(b_{0,2}^{+}\big) - \arg\big(\mathfrak{b}_{0,1}^{+}\big)}{2}. \tag{D4d}$$

Appendix E. Details of bound *IG* wave surface elevations

Details of quantities in (2.14) are given. The bound *IG* waves due to self-interactions between diffracted carrier waves, and self-interactions between radiated carrier waves in regions I and III are

$$\eta_{bIG}^{\mathrm{I},D_1D_2} = 2\big(C_1+C_2\big)\big|a_{0,1}^{-}\big\|a_{0,2}^{-}\big|\cos\big[2\big(-k_L(X+L)-\omega_L T+\gamma_{IG}^{\mathrm{I},D_1D_2}\big)\big], \tag{E1a}$$

$$\eta_{bIG}^{\mathrm{I},R_1R_2} = 2\big(C_1+C_2\big)\big|\mathfrak{a}_{0,1}^{-}\big\|\mathfrak{a}_{0,2}^{-}\big|\cos\big[2\big(-k_L(X+L)-\omega_L T+\gamma_{IG}^{\mathrm{I},R_1R_2}\big)\big], \tag{E1b}$$

$$\eta_{bIG}^{\mathrm{III},D_1D_2} = 2\big(C_1+C_2\big)\big|b_{0,1}^{+}\big\|b_{0,2}^{+}\big|\cos\big[2\big(k_L(X-L)-\omega_L T+\gamma_{IG}^{\mathrm{III},D_1D_2}\big)\big], \tag{E1c}$$

$$\eta_{bIG}^{\mathrm{III},R_1R_2} = 2\big(C_1+C_2\big)\big|\mathfrak{b}_{0,1}^{+}\big\|\mathfrak{b}_{0,2}^{+}\big|\cos\big[2\big(k_L(X-L)-\omega_L T+\gamma_{IG}^{\mathrm{III},R_1R_2}\big)\big], \tag{E1d}$$

where the phase angles $\gamma_{IG}^{\mathrm{I},D_1D_2}$ etc. are defined by (D2) and (D4). The bound *IG* waves due to cross-interactions between diffracted and radiated carrier waves in regions I and III are

$$\eta_{bIG}^{\mathrm{I},D_1R_2} = 2\big(C_1+C_2\big)\big|a_{0,1}^{-}\big\|\mathfrak{a}_{0,2}^{-}\big|\cos\big[2\big(-k_L(X+L)-\omega_L T+\gamma_{IG}^{\mathrm{I},D_1R_2}\big)\big], \tag{E2a}$$

$$\eta_{bIG}^{\mathrm{I},D_2R_1} = 2\big(C_1+C_2\big)\big|a_{0,2}^{-}\big\|\mathfrak{a}_{0,1}^{-}\big|\cos\big[2\big(-k_L(X+L)-\omega_L T+\gamma_{IG}^{\mathrm{I},D_2R_1}\big)\big], \tag{E2b}$$

$$\eta_{bIG}^{\mathrm{III},D_1R_2} = 2\big(C_1+C_2\big)\big|b_{0,1}^{+}\big\|\mathfrak{b}_{0,2}^{+}\big|\cos\big[2\big(k_L(X-L)-\omega_L T+\gamma_{IG}^{\mathrm{III},D_1R_2}\big)\big], \tag{E2c}$$

$$\eta_{bIG}^{\mathrm{III},D_2R_1} = 2\big(C_1+C_2\big)\big|b_{0,2}^{+}\big\|\mathfrak{b}_{0,1}^{+}\big|\cos\big[2\big(k_L(X-L)-\omega_L T+\gamma_{IG}^{\mathrm{III},D_2R_1}\big)\big]. \tag{E2d}$$

Appendix F. Details of equations arising from matching conditions

This section provides details for § 5. Submitting known quantities into (5.3–5.6) and collecting like harmonics to obtain eight equations for eight unknowns D^{I}, D^{III}, $\overline{D^{\mathrm{I}}}$, $\overline{D^{\mathrm{III}}}$,

https://doi.org/10.1017/jfm.2025.10514 Published online by Cambridge University Press

$\mathcal{A}_1$, $\mathcal{A}_2$, $\overline{\mathcal{A}_1}$ and $\overline{\mathcal{A}_2}$. The phase angles $\gamma_{IG}^{\mathrm{I},D_1D_2}$ *etc.* below are defined by (D2) and (D4)

$$-C_B\left(\mathrm{e}^{-2\mathrm{i}k_LX}A_1A_2+\mathrm{e}^{-2\mathrm{i}\gamma_{IG}^{\mathrm{I},D_1D_2}}\left|a_{0,1}^-\right\|a_{0,2}^-\right|+\mathrm{e}^{-2\mathrm{i}\gamma_{IG}^{\mathrm{I},R_1R_2}}\left|\mathfrak{a}_{0,1}^-\right\|\mathfrak{a}_{0,2}^-\right| + \mathrm{e}^{-2\mathrm{i}\gamma_{IG}^{\mathrm{I},D_1R_2}}\left|a_{0,1}^-\right\|\mathfrak{a}_{0,2}^-\right|+\mathrm{e}^{-2\mathrm{i}\gamma_{IG}^{\mathrm{I},D_2R_1}}\left|a_{0,2}^-\right\|\mathfrak{a}_{0,1}^-\right|\Big)+\overline{D^{\mathrm{I}}}\mathrm{e}^{2\mathrm{i}\frac{\omega_L}{\sqrt{gh}}X}=\overline{\mathcal{A}}_1x+\overline{\mathcal{A}}_2\big|_{X=-L}, \tag{F1}$$

$$C_B\left(\mathrm{e}^{2\mathrm{i}k_LX}A_1A_2+\mathrm{e}^{2\mathrm{i}\gamma_{IG}^{\mathrm{I},D_1D_2}}\left|a_{0,1}^-\right\|a_{0,2}^-\right|+\mathrm{e}^{2\mathrm{i}\gamma_{IG}^{\mathrm{I},R_1R_2}}\left|\mathfrak{a}_{0,1}^-\right\|\mathfrak{a}_{0,2}^-\right| + \mathrm{e}^{2\mathrm{i}\gamma_{IG}^{\mathrm{I},D_1R_2}}\left|a_{0,1}^-\right\|\mathfrak{a}_{0,2}^-\right|+\mathrm{e}^{2\mathrm{i}\gamma_{IG}^{\mathrm{I},D_2R_1}}\left|a_{0,2}^-\right\|\mathfrak{a}_{0,1}^-\right|\Big)+D^{\mathrm{I}}\mathrm{e}^{-2\mathrm{i}\omega_L/\sqrt{gh}X}=\mathcal{A}_1x+\mathcal{A}_2\big|_{X=-L}, \tag{F2}$$

$$2\mathrm{i}k_LC_B\left(\mathrm{e}^{-2\mathrm{i}k_LX}A_1A_2-\mathrm{e}^{-2\mathrm{i}\gamma_{IG}^{\mathrm{I},D_1D_2}}\left|a_{0,1}^-\right\|a_{0,2}^-\right|-\mathrm{e}^{-2\mathrm{i}\gamma_{IG}^{\mathrm{I},R_1R_2}}\left|\mathfrak{a}_{0,1}^-\right\|\mathfrak{a}_{0,2}^-\right| - \mathrm{e}^{-2\mathrm{i}\gamma_{IG}^{\mathrm{I},D_1R_2}}\left|a_{0,1}^-\right\|\mathfrak{a}_{0,2}^-\right|-\mathrm{e}^{-2\mathrm{i}\gamma_{IG}^{\mathrm{I},D_2R_1}}\left|a_{0,2}^-\right\|\mathfrak{a}_{0,1}^-\right|+\frac{\omega_L\overline{D^{\mathrm{I}}}\mathrm{e}^{2\mathrm{i}\omega_{\mathrm{L}}/\sqrt{gh}X}}{k_LC_B\sqrt{gh}}\Big)=\overline{\mathcal{A}}_1\big|_{X=-L}, \tag{F3}$$

$$2\mathrm{i}k_LC_B\left(\mathrm{e}^{2\mathrm{i}k_LX}A_1A_2-\mathrm{e}^{2\mathrm{i}\gamma_{IG}^{\mathrm{I},D_1D_2}}\left|a_{0,1}^-\right\|a_{0,2}^-\right|-\mathrm{e}^{2\mathrm{i}\gamma_{IG}^{\mathrm{I},R_1R_2}}\left|\mathfrak{a}_{0,1}^-\right\|\mathfrak{a}_{0,2}^-\right| - \mathrm{e}^{2\mathrm{i}\gamma_{IG}^{\mathrm{I},D_1R_2}}\left|a_{0,1}^-\right\|\mathfrak{a}_{0,2}^-\right|-\mathrm{e}^{2\mathrm{i}\gamma_{IG}^{\mathrm{I},D_2R_1}}\left|a_{0,2}^-\right\|\mathfrak{a}_{0,1}^-\right|-\frac{\omega_L\overline{D^{\mathrm{I}}}\mathrm{e}^{-2\mathrm{i}\omega_{\mathrm{L}}/\sqrt{gh}X}}{k_LC_B\sqrt{gh}}\Big)=\mathcal{A}_1\big|_{X=-L}, \tag{F4}$$

$$\overline{\mathcal{A}}_1x+\overline{\mathcal{A}}_2=-C_B\mathrm{e}^{-2\mathrm{i}\gamma_{IG}^{\mathrm{III},D_1D_2}}\left|b_{0,1}^+\right\|b_{0,2}^+\right|-C_B\mathrm{e}^{-2\mathrm{i}\gamma_{IG}^{\mathrm{III},R_1R_2}}\left|\mathfrak{b}_{0,1}^+\right\|\mathfrak{b}_{0,2}^+\right| - C_B\mathrm{e}^{-2\mathrm{i}\gamma_{IG}^{\mathrm{III},D_1R_2}}\left|b_{0,1}^+\right\|\mathfrak{b}_{0,2}^+\right|-C_B\mathrm{e}^{-2\mathrm{i}\gamma_{IG}^{\mathrm{III},D_2R_1}}\left|b_{0,2}^+\right\|\mathfrak{b}_{0,1}^+\right|+\overline{D^{\mathrm{III}}}\mathrm{e}^{-2\mathrm{i}\omega_{\mathrm{L}}/\sqrt{gh}X}\big|_{X=L}, \tag{F5}$$

$$\mathcal{A}_1x+\mathcal{A}_2=C_B\mathrm{e}^{2\mathrm{i}\gamma_{IG}^{\mathrm{III},D_1D_2}}\left|b_{0,1}^+\right\|b_{0,2}^+\right|+C_B\mathrm{e}^{2\mathrm{i}\gamma_{IG}^{\mathrm{III},R_1R_2}}\left|\mathfrak{b}_{0,1}^+\right\|\mathfrak{b}_{0,2}^+\right| + C_B\mathrm{e}^{2\mathrm{i}\gamma_{IG}^{\mathrm{III},D_1R_2}}\left|b_{0,1}^+\right\|\mathfrak{b}_{0,2}^+\right|+C_B\mathrm{e}^{2\mathrm{i}\gamma_{IG}^{\mathrm{III},D_2R_1}}\left|b_{0,2}^+\right\|\mathfrak{b}_{0,2}^+\right|+D^+\mathrm{III}\mathrm{e}^{2\mathrm{i}\omega_{\mathrm{L}}/\sqrt{gh}X}\big|_{X=L}, \tag{F6}$$

$$\overline{\mathcal{A}}_1=2\mathrm{i}k_{\mathrm{L}}C_B\left(\mathrm{e}^{-2\mathrm{i}\gamma_{IG}^{\mathrm{III},D_1D_2}}\left|b_{0,1}^+\right\|b_{0,2}^+\right|+\mathrm{e}^{-2\mathrm{i}\gamma_{IG}^{\mathrm{III},R_1R_2}}\left|\mathfrak{b}_{0,1}^+\right\|\mathfrak{b}_{0,2}^+\right| + \mathrm{e}^{-2\mathrm{i}\gamma_{IG}^{\mathrm{III},D_1R_2}}\left|b_{0,1}^+\right\|\mathfrak{b}_{0,2}^+\right|+\mathrm{e}^{-2\mathrm{i}\gamma_{IG}^{\mathrm{III},D_2R_1}}\left|b_{0,2}^+\right\|\mathfrak{b}_{0,1}^+\right|-\frac{\omega_{\mathrm{L}}\overline{D^{\mathrm{III}}}\mathrm{e}^{-2\mathrm{i}\omega_{\mathrm{L}}/\sqrt{gh}X}}{k_LC_B\sqrt{gh}}\Big)\big|_{X=L}, \tag{F7}$$

https://doi.org/10.1017/jfm.2025.10514 Published online by Cambridge University Press

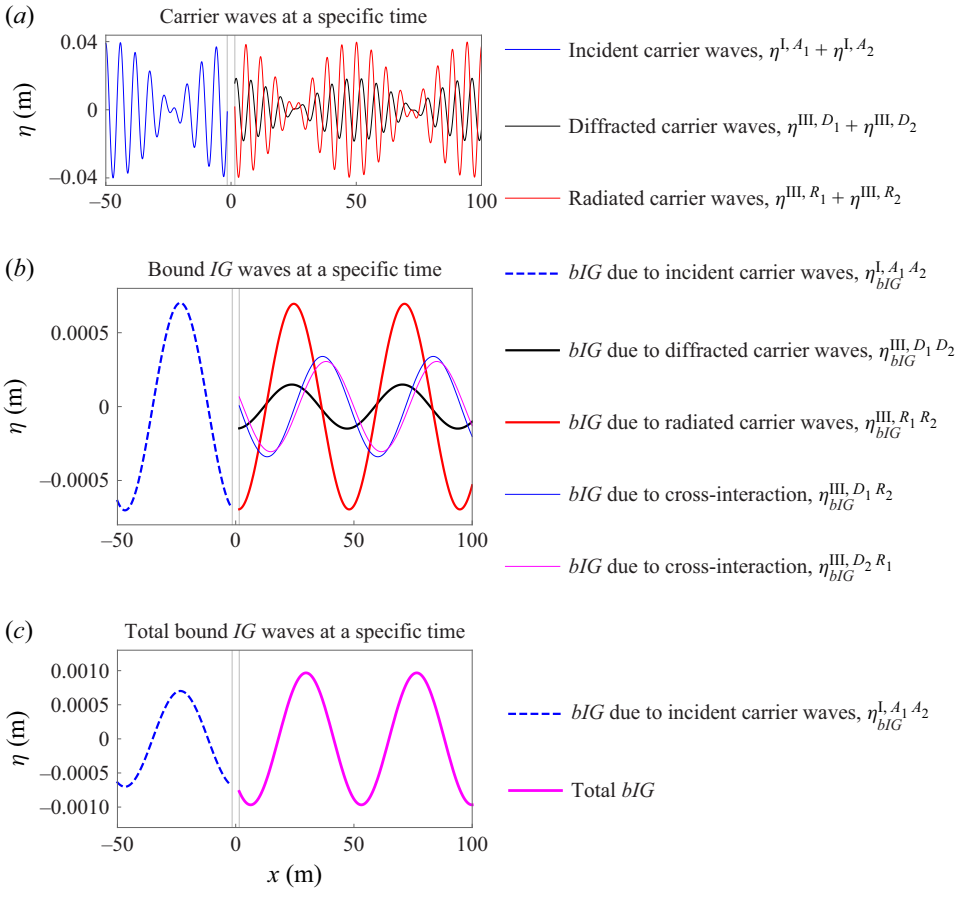


Figure 13. The total bound *IG* waves can be higher than the incident bound *IG* wave. The case corresponds to a case on the black curves in the fourth column of figure 7 where $L=1.5h$, $d=0.1h$, $h=1$ m, $k_{0,1}h=1$. Surface elevation η for: (*a*) carrier waves; (*b*) bound *IG* waves; (*c*) total bound *IG* waves. Free *IG* waves are not shown, because this figure focuses only on bound *IG* waves. This figure corresponds to Appendix G.

$$\mathcal{A}_1 = 2\mathrm{i}k_L C_B \left(\mathrm{e}^{2\mathrm{i}\gamma_{IG}^{\mathrm{III},D_1D_2}} \left|b_{0,1}^{+}\right\|b_{0,2}^{+}\right| + \mathrm{e}^{2\mathrm{i}\gamma_{IG}^{\mathrm{III},R_1R_2}} \left|\mathfrak{b}_{0,1}^{+}\right\|\mathfrak{b}_{0,2}^{+}\right| + \mathrm{e}^{2\mathrm{i}\gamma_{IG}^{\mathrm{III},D_1R_2}} \left|b_{0,1}^{+}\right\|\mathfrak{b}_{0,2}^{+}\right| + \mathrm{e}^{2\mathrm{i}\gamma_{IG}^{\mathrm{III},D_2R_1}} \left|b_{0,2}^{+}\right\|\mathfrak{b}_{0,1}^{+}\right| + \frac{\omega_L D^{\mathrm{III}} \mathrm{e}^{2\mathrm{i}\omega_L/\sqrt{gh}X}}{k_L C_B \sqrt{gh}} \Bigg) \Big|_{X=L}. \tag{F8}$$

Appendix G. Increased bound *IG* waves

This appendix explains why the total bound *IG* waves in panels (*m*), (*n*), (*o*) of figure 7 can be greater than the incident bound *IG* waves. Consider an example taken from the black curve in figure 7(*n*) where $L=h$, $d=0.1h$. Further choose $k_{0,1}h=1$. In this case, the amplitude of $\eta_{bIG}^{\mathrm{III},tot}$ is greater than the incident *IG* waves. Carrier waves (incident, radiated and diffracted) are plotted in figure 13(*a*), and bound *IG* waves are plotted in figure 13(*b*). Although the phase shift between radiated and diffracted carrier waves is large, such that they destructively superimpose, the same cannot be said for bound *IG*

https://doi.org/10.1017/jfm.2025.10514 Published online by Cambridge University Press

waves: there is almost zero phase shift between $\eta_{bIG}^{\mathrm{III},R_1R_2}$ (red) and $\eta_{bIG}^{\mathrm{III},D_1D_2}$ (black), such that they superimpose constructively, leading to total *IG* waves larger than the incident *IG* waves. The remaining two *IG* wave components, *viz.* the blue- and the magenta-coloured waves, are $\eta_{bIG}^{\mathrm{I},D_1R_2}$ and $\eta_{bIG}^{\mathrm{I},D_2R_1}$ (due to cross-interactions). Although they are no longer in phase with the aforementioned two waves, they cannot override the overall result that the total bound *IG* wave is larger than the incident counterpart, see figure 13(*c*). This suggests that for the heaving cases, the superposition of bound *IG* wave components does not necessarily repeat the way carrier waves superimpose: it is possible that while carrier waves destructively superimpose, the bound *IG* wave components can constructively superimpose, giving rise to greater total *IG* waves.

References

Agnon, Y., Choi, H.S. & Mei, C.C. 1988 Slow drift of a floating cylinder in narrow-banded beam seas. *J. Fluid Mech.* **190**, 141–163.

Agnon, Y. & Mei, C.C. 1985 Slow-drift motion of a two-dimensional block in beam seas. *J. Fluid Mech.* **151**, 279–294.

Ardhuin, F., Rawat, A. & Aucan, J. 2014 A numerical model for free infragravity waves: definition and validation at regional and global scales. *Ocean Model.* **77**, 20–32.

Bennetts, L.G., Liang, J. & Pitt, J.P.A. 2022 Modeling ocean wave transfer to Ross ice shelf flexure. *Geophys. Res. Lett.* **49** (21), e2022GL100868.

Benney, D.J. & Roskes, G.J. 1969 Wave instabilities. *Stud. Appl. Maths* **48** (4), 377–385.

Bertin, X. *et al.*et al. 2018 Infragravity waves: from driving mechanisms to impacts. *Earth-Sci. Rev.* **177**, 774–799.

Bowers, E.C. 1977 Harbour resonance due to set-down beneath wave groups. *J. Fluid Mech.* **79** (1), 71–92.

Cui, L., Manasseh, R., Leontini, J.S. & Tothova, D. 2022 Nonlinearities in the dynamics of reciprocating pipe flow in relation to oscillating water column wave energy converters. In Australasian Fluid Mechanics Conference (AFMC)

Cui, L., Sergiienko, N.Y., Cazzolato, B., Leontini, J.S., Tothova, D., Cannard, P., Spinks, N. & Manasseh, R. 2023 On using Helmholtz-type resonance to reduce the size of dual-purpose offshore oscillating water column wave energy converters. *Phys. Fluids* **35** (9), 097110.

Elgar, S., Herbers, T.H.C., Okihiro, M., Oltman-Shay, J. & T.Guza, R. 1992 Observations of infragravity waves. *J. Geophys. Res. Oceans* **97** (C10), 15573–15577.

Falnes, J. & Budal, K. 1982 Wave-power absorption by parallel rows of interacting oscillating bodies. *Appl. Ocean Res.* **4** (4), 194–207.

Falnes, J. & Kurniawan, A. 2020 *Ocean Waves and Oscillating Systems: Linear Interactions Including Wave-Energy Extraction*. Cambridge University Press.

Gao, J., Ma, X., Dong, G., Chen, H., Liu, Q. & Zang, J. 2021 Investigation on the effects of Bragg reflection on harbor oscillations. *Coastal Engng* **170**, 103977.

Hermans, A.J. 2010 *Water Waves and Ship Hydrodynamics: An Introduction*. Springer Science & Business Media.

Hossain, A., Kioka, W. & Kitano, T. 2001 Transmission of long waves induced by short-wave groups through a composite breakwater. *Coastal Engng J.* **43** (02), 83–97.

Lee, L.-F. 1995 On the heave radiation of a rectangular structure. *Ocean Engng* **22** (1), 19–34.

Li, Y., Zheng, Y., Lin, Z., Adcock, T.A.A. & van den Bremer, T.S. 2021 Surface wavepackets subject to an abrupt depth change. Part 1. Second-order theory. *J. Fluid Mech.* **915**, A71.

Linton, C.M. & McIver, P. 2001 *Handbook of Mathematical Techniques for Wave/Structure Interactions*. Chapman and Hall/CRC.

Liu, P.L.-F. & Iskandarani, M. 1991 Scattering of short-wave groups by submerged horizontal plate. *J. Waterway Port Coastal Ocean Engng* **117** (3), 235–246.

Longuet-Higgins, M.S. & Stewart, R.W. 1962 Radiation stress and mass transport in gravity waves, with application to 'surf beats'. *J. Fluid Mech.* **13** (4), 481–504.

Losada, M.A., Losada, I.J. & Roldán, A.J. 1993 Propagation of oblique incident modulated waves past rigid, vertical thin barriers. *Appl. Ocean Res.* **15** (5), 305–310.

Manasseh, R. 2021 *Fluid Waves*. CRC Press.

Massel, S.R. 1983 Harmonic generation by waves propagating over a submerged step. *Coastal Engng* **7** (4), 357–380.

https://doi.org/10.1017/jfm.2025.10514 Published online by Cambridge University Press

McComb, P.J., Johnson, D.L. & Beamsley, B.J. 2009 Numerical study of options to reduce swell and long wave penetration at Port Geraldton. In *Coasts and Ports 2009: In a Dynamic Environment*, pp. 490–496. Engineers Australia.

McCormick, M.E. 2009 *Ocean Engineering Mechanics: with Applications*. Cambridge University Press.

Mei, C.C. & Agnon, Y. 1989 Long-period oscillations in a harbour induced by incident short waves. *J. Fluid Mech.* **208**, 595–608.

Mei, C.C. & Benmoussa, C. 1984 Long waves induced by short-wave groups over an uneven bottom. *J. Fluid Mech.* **139**, 219–235.

Mei, C.C., Stiassnie, M.A. & Yue, D.K.-P. 2005 *Theory and Applications of Ocean Surface Waves: Part 2: Nonlinear Aspects*. World Scientific.

Neves, M.G., Losada, I.J. & Losada, M.A. 2000*a* Propagation of incident modulated waves past impermeable semi-infinite breakwaters. *Appl. Ocean Res.* **22** (1), 55–60.

Neves, M.G., Losada, I.J. & Losada, M.A. 2000*b* Short-wave and wave group scattering by submerged porous plate. *J. Engng Mech* **126** (10), 1048–1056.

Sergiienko, N.Y., Cannard, P.A., Cui, L., Leontini, J.S., Manasseh, R. & Cazzolato, B. 2024 Impact of wave energy converters on infragravity waves: an experimental investigation. *Ocean Engng* **309**, 118345.

Sheng, W., Alcorn, R. & Lewis, A. 2014 Assessment of primary energy conversions of oscillating water columns. I. Hydrodynamic analysis. *J. Renew. Sustain. Energy* **6** (5), 053113.

Srokosz, M.A. 1980 Some relations for bodies in a canal, with an application to wave-power absorption. *J. Fluid Mech.* **99** (1), 145–162.

Westcott, A.-R., Bennetts, L.G., Sergiienko, N.Y. & Cazzolato, B.S. 2024 Broadband near-perfect capture of water wave energy by an array of heaving buoy wave energy converters. *J. Fluid Mech.* **998**, A5.

Wu, J.-K. & Liu, P.L.-F. 1990 Harbour excitations by incident wave groups. *J. Fluid Mech.* **217**, 595–613.

Yiew, L.J. 2017 Modelling the wave-induced collisions of ice floes. *PhD thesis*, The University of Adelaide, Adelaide, Australia.

https://doi.org/10.1017/jfm.2025.10514 Published online by Cambridge University Press